DISSERTATIONS IN
FORESTRY AND
NATURAL SCIENCES

Jussi Rahomäki

Subwavelength photonics for enhanced optical imaging

Publications of the University of Eastern Finland
Dissertations in Forestry and Natural Sciences No 117

UNIVERSITY OF
EASTERN FINLAND

JUSSI RAHOMÄKI

Subwavelength photonics for enhanced optical imaging

Publications of the University of Eastern Finland
Dissertations in Forestry and Natural Sciences
No 117

Academic Dissertation
To be presented by permission of the Faculty of Science and Forestry for public examination in the Auditorium M103 in Metria Building at the University of Eastern Finland, Joensuu, on August, 30, 2013,
at 12 o'clock noon.

Department of Physics and Mathematics

Kopijyvä Oy
Joensuu, 2013
Editor: Prof. Pertti Pasanen, Prof. Pekka Kilpeläinen, Prof. Kai Peiponen,
Prof. Matti Vornanen

Distribution:
University of Eastern Finland Library / Sales of publications
julkaisumyynti@uef.fi
http://www.uef.fi/kirjasto

ISBN: 978-952-61-1192-6 (printed)
ISSNL: 1798-5668
ISSN: 1798-5668
ISBN: 978-952-61-1193-3 (pdf)
ISSNL: 1798-5668
ISSN: 1798-5676

Author's address:
University of Eastern Finland
Department of Physics and Mathematics
P.O.Box 111
80101 JOENSUU
FINLAND
email: rahomaki@kth.se

Supervisors:
Professor Jari Turunen, Ph.D.
University of Eastern Finland
Department of Physics and Mathematics
P.O.Box 111
80101 Joensuu
FINLAND
email: jari.turunen@uef.fi

Professor Pasi Vahimaa, Ph.D.
University of Eastern Finland
Department of Physics and Mathematics
P.O.Box 111
80101 Joensuu
FINLAND
email: pasi.vahimaa@uef.fi

Reviewers:
Professor Vilson Rosa de Almeida, Ph.D.
Instituto de Estudos Avançados
Divisão de Fotônica
Caixa Postal 6044
12228-001 São José dos Campos, SP
BRAZIL
email: vilson@ieav.cta.br

Antti Säynätjoki, Docent, D.Sc.
Aalto University
Department of Micro and Nanosciences
P.O.Box 13500
00076 Aalto
FINLAND
email: antti.saynatjoki@aalto.fi

Opponent:
Professor Carsten Rockstuhl, Ph.D.
Friedrich Schiller University Jena
Institute of Condensed Matter and Solid State Optics
Max-Wien-Plaz 1
07743 Jena
GERMANY

ABSTRACT

This thesis consists of numerical and experimental studies on subwavelength photonics for various optical imaging schemes. Methods for enhancing sensitivity and resolution of photonic devices are considered in fields of fluorescence imaging, Raman scattering, optoacoustics, and free-field detection.

Metallic and dielectric structures, along with their combinations, are considered in this work. A main concept is resonance waveguide grating (RWG) which either alone or with functional metallic surfaces is employed in fluorescence detection sensitivity enhancement, Raman scattering enhancement, and high resolution optoacoustic surface wave excitation. In addition, a metallic nanoaperture is studied as a potential high resolution free-field sensor based on extraordinary transmission in subwavelength size aperture.

Numerical investigations are carried out by electromagnetically fully rigorous Fourier Modal Method (FMM) which enables highly detailed simulations of the studied interactions. Advanced nanofabrication techniques are implemented to fabricate the structures, including electron beam and nanoimprint lithography, dry etching, and thin film deposition techniques. Experimental proofs are discussed for fluorescence and Raman enhancements as well as for free-field sensing.

Highlighting shortly the most remarkable results shown in this thesis: We have demonstrated more than 500-fold enhancement in laser induced fluorescence signal using resonance waveguide grating and further, using the similar approach, more than 30-fold enhancement in fluorescence signal in conventional fluorescence microscopy. Moreover, we have demonstrated a new type of horizontal slot waveguide device to significantly enhance Raman signal detection from nanochannels. Finally, we have shown a promising approach for direct characterization of focal-region optical fields with subwavelength-scale structure.

Universal Decimal Classification: 535.42, 537.874.3, 537.876.4, 681.7.02, 681.7.063, 681.7.064
PACS Classification: 42.25.-p, 42.79.-e, 42.82-m, 87.64.-t
Library of Congress Subject Headings: Optics; Photonics; Imaging systems; Raman effect; Optical detectors; Acoustooptics; Fluorescence; Microfabrication; Lithography, Electron beam; Nanostructured materials; Metals; Dielectrics; Optical waveguides; Optical resonance; Numerical analysis;
Yleinen suomalainen asiasanasto: optiikka; optiset laitteet; kuvantaminen; optiset anturit; fluoresenssi; mikrotekniikka; mikrorakenteet; nanorakenteet; litografia; numeerinen analyysi;

Preface

First of all, I wish to thank my supervisors Jari Turunen and Pasi Vahimaa for guiding me through out my studies. In addition, many thanks to Seppo Honkanen who contributed a lot to my work, though not being officially a supervisor. Yet, I would like to thank all the co-authors to shearing scientific interests and knowledge with me.

I would also like to thank professor Arto Nurmikko, under whose guidance I got a great chance to spend the highly educating year in Brown University. Big thanks belong also to many of the Brown people, especially Cuong, Joonhee, Michael, Dave, Ben, Don and Anton. Similarly, I am grateful to Shakil Rehman of Singapore-MIT Alliance for Research and Technology to allow me to spend some time in their lab for the experimental work of the last paper in this work.

I greatly appreciate the support of all the colleagues in Joensuu who I worked with. To name a few, I especially like to thank Janne Laukkanen for the all uncountable hours we spent to solve problems related to fabrication issues, Petri Karvinen for the inspiring guidance in the very beginning of my researcher career, as well as Risto, Mikko, Kalle, Ismo, and Petri for the relaxing atmosphere in the work and often also outside the work.

Finally, I would like to thank my wife Krista for all the support and understanding of our moving life around the globe.

Stockholm 17 July, 2013 *Jussi Rahomäki*

LIST OF PUBLICATIONS

This thesis consists of the present review of the author's work in the field of photonics and the following selection of the author's publications:

I P. Karvinen, T. Nuutinen, J. Rahomäki, O. Hyvärinen, and P. Vahimaa, "Strong fluorescence-signal gain with single-excitation-enhancing and emission-directing nanostructured diffraction grating," *Opt. Lett.* **34,** 3208–3210 (2009). (With the permission of OSA)

II T. Nuutinen, P. Karvinen, J. Rahomäki, and P. Vahimaa, "Resonant waveguide grating (RWG): Overcoming the problem of angular sensitivity by conical, broad-band illumination for fluorescence measurements," *Anal. Methods* **5,** 281–284 (2013). (With the permission of RSC)

III J. Rahomäki, T. Nuutinen, L. Karvonen, S. Honkanen, and P. Vahimaa, "Horizontal slot waveguide channel for enhanced Raman scattering," *Opt. Express* **21,** 9060–9068 (2013). (With the permission of OSA)

IV J. Rahomäki, H.J. Hyvärinen, S. Rehman, and J. Turunen, "Free-field characterization via directional transmission through a nanoaperture," *Nanoscale Res. Lett.* **8,** 326 (2013). (With the permission of Springer)

Throughout the overview, these papers will be referred to by Roman numerals.

AUTHOR'S CONTRIBUTION

The publications selected in this dissertation are original research papers on enhanced optical imaging.

The author has significantly participated in the experimental work and data analysis for Papers **I**, **III**, and **IV**. The fabrication of the structures for Papers **III** and **IV** was fully done by the author. The author has carried out all the numerical calculations in Paper **III** and has significantly participated in the numerical analysis in publications **II** and **IV**. The author has written the manuscript in Paper **III**, partially written the manuscript in Paper **IV**, and participated in the writing processes of the manuscripts in Papers **I** and **II**. The author introduced the idea for Paper **III** and was involved with the co-authors in inventing the ideas for the other papers.

The papers have been completed with significant co-operation with the co-authors.

Contents

1 Introduction

In conventional microscopy techniques, the spatial resolution is fundamentally limited by diffraction. This was realized by Ernst Abbe in 1873 whose findings determined that it is not possible to resolve two objects that are closer than $\lambda/2NA$, where NA is the numerical aperture of the system and λ is the wavelength of light. This finding ruled the field of optical imaging until recently an extensive number of techniques has pushed the limit far beyond the diffraction limit [1–10].

Modern optical imaging has outstandingly made use of plasmonic phenomena that also have significant importance in a wide range of applications outside of imaging systems such as solar cell technology [11, 12], health sciences [13–15], and environmental sciences [16] to name but a few. Various surface plasmon based imaging or imaging assisting methods have been developed including biosensors [17–19], super resolution plasmonic lenses [20–22], surface enhanced Raman scattering platforms [23–25], extraordinary transmission [26–29], and optical trapping [30, 31] among others.

Alternatively, dielectric subwavelength structures can be employed to control the electromagnetic field with high precision. Notably, slot-waveguides [32–34] and various waveguide resonance approaches [35–37] have an importance in sensing applications.

Another limiting aspect in the conventional microscopy is the light scattering that reduces the mean free path of a photon and thus restricts the imaging ability of thick, partially transparent, samples such as a biological tissue. The mean free path describes an average distance that a photon travels between two successive scattering events. The most widely used methods in deep tissue imaging are multiphoton [38] and confocal microscopy [39] which, however, provide only a moderate improvement in the imaging depth [40]. Significantly enhanced imaging depth with resolution down to a few microns can be achieved by optical coherence to-

mography (OCT) [41]. Also, photoacoustic microscopy provides a possible approach to overcome the penetration depth based limitations [42, 43]. A drawback of the enhanced imaging depth has been a loss in the spatial resolution but recently this has been shown to be possible to overcome by tightly focused exciting light [44, 45]. The high spatial resolution optoacoustic detection has a strong potential in the field of nanometrology where non-invasive methods are deliberately wanted [46].

In the point of view of fabricating subwavelength scale structures, it has been possible to achieve rather small features already for quite a while by following the development of decreasing feature sizes in semiconductor technology [47]. However, not any desired structure or material is manageable in nanoscale fabrication with same efficiency and robustness as manufacturing of a silicon component for an integrated circuit. Nevertheless, recent development of lithographic tools and resist technologies has a great impact also in photonics applications. Very recently, it has been possible to achieve sub-10 nanometer features through several types of process choices [25, 48, 49].

This doctoral thesis is divided into eight chapters. After introduction, Chapter 2 introduces the objectives of this study. Chapter 3 summarizes methods used to analyze electromagnetic field interactions in subwavelength structures and the most relevant light-matter interactions dealt within this thesis. Principal nanofabrication methods are discussed in Chapter 4. Chapter 5 gives an overview of resonance waveguide grating based fluorescent emission enhancement methods, presented in Papers **I** and **II**. Also, as yet unpublished results on electric dipole scattering in the near field of a resonance waveguide grating are discussed. Advantages of combining the resonance waveguide grating with a functional metal surface are discussed in Chapter 6, including results published in Paper **III** for enhanced Raman detection and unpublished results in optoacoustic surface wave excitation. The précis of Paper **IV** that demonstrate an extraordinary transmission based detection method is given in Chapter 7. The final conclusions are given in Chapter 8

along with an outlook for future research directions.

2 Objectives

In this thesis, potential approaches for enhanced optical imaging are investigated. Particularly, advances in detection sensitivity and resolution are studied by means of subwavelength photonics.

The following four main categories define the objectives of this thesis. The categories are:

1. To enhance fluorescence detection sensitivity using tailored dielectric surfaces with subwavelength scale modulation. Scattering of an electric dipole in vicinity of a such surface is also investigated numerically as an approximative model of a fluorescent emitting molecule.

2. To enhance Raman scattering detection sensitivity from nanoscale channels by employing tailored dielectric and metallic surfaces with subwavelength modulation.

3. To study subwavelength structures in efficient and high resolution optical excitation of acoustic surface waves by controlling intensity modulation of the exciting light energy.

4. To investigate methods for high resolution free-field characterization using surface plasmon assisted transmission through a nanoaperture.

In all the categories the objectives involve work in simulations, fabrication, and experimental measurements.

3 Field interaction in sub-wavelength structures

Describing electromagnetic field behavior in subwavelength sized structures requires treating the interaction of light and matter in a wave form. Propagation of the light in such small structures does not allow to treat it by means of geometrical optics and in many cases neither an approximative model is usable.

However, an accurate characterization of subwavelength structures provides keys to take great advantages out of the strictly controlled electromagnetic field behavior. In this chapter, a brief background for the theory behind the scope of the work is given. It does not aim to be complete but rather guide a reader to the concept of this work. A short introduction to the wave theory of diffraction gratings and their analysis is given. In addition, the most relevant interaction methods of the light and matter are described, including fluorescence, Raman scattering, plasmonic resonance, and optically excited acoustic waves.

3.1 IDEAL OPTICAL FIELD

Here we consider a monochromatic time-harmonic field of the form

$$\begin{aligned} \boldsymbol{U}_{\mathrm{re}}(\boldsymbol{r},t) &= \Re\{\boldsymbol{U}(\boldsymbol{r})\exp(-\mathrm{i}\omega t)\} \\ &= \frac{1}{2}[\boldsymbol{U}(\boldsymbol{r})\exp(-\mathrm{i}\omega t) + \boldsymbol{U}^{*}(\boldsymbol{r})\exp(\mathrm{i}\omega t)], \end{aligned} \tag{3.1}$$

where $\boldsymbol{U}(\mathbf{r})$ is a complex representation of a real valued function $\boldsymbol{U}_{\mathrm{re}}(\mathbf{r},\mathrm{t})$ and it is replaced by either an electric field $\boldsymbol{E}(\boldsymbol{r})$ or a magnetic field $\boldsymbol{H}(\boldsymbol{r})$ in further discussion. The asterisk denotes the complex conjugate and the variables $\boldsymbol{r}, \omega, t$ represent the position vector, angular frequency, and time respectively.

The radiation emitted by a primary source may be described as a superposition of harmonic waves. A harmonic field is defined by angular frequency ω. This is sufficient, albeit not completely correct, to describe a single optical mode. However, such single mode appears in many lasers, waveguides and optical fibers to name a few.

Even if an ideal optical field does never exist in the real world, it may provide a sufficiently good approximation in many cases without a need to take into account the manifold coherence properties that are the nature of realistic optical fields in the more general sense [50]. This, of course, is always the question of a purpose of an optical design or simulation.

Let us consider a harmonic field in a homogenous medium and a well known Helmholtz equation pair [51]

$$\nabla^2 \boldsymbol{E}(\boldsymbol{r}) + k^2 \boldsymbol{E}(\boldsymbol{r}) = 0 \tag{3.2}$$

and

$$\nabla^2 \boldsymbol{H}(\boldsymbol{r}) + k^2 \boldsymbol{H}(\boldsymbol{r}) = 0, \tag{3.3}$$

where

$$k = \omega/v = n\omega/c = k_0 n. \tag{3.4}$$

The quantity k is known as the wave number of the harmonic electromagnetic field in the medium with refractive index n, and k_0 is the wave number in vacuum.

The simplest solution of the equations (3.2) and (3.3) is

$$\boldsymbol{E}(\boldsymbol{r}) = \boldsymbol{E}_0 \exp(\mathrm{i}\boldsymbol{k} \cdot \boldsymbol{r}), \tag{3.5}$$

$$\boldsymbol{H}(\boldsymbol{r}) = \boldsymbol{H}_0 \exp(\mathrm{i}\boldsymbol{k} \cdot \boldsymbol{r}), \tag{3.6}$$

where $\boldsymbol{k}$ is the wave vector with $|\boldsymbol{k}| = k$,

$$\boldsymbol{H}_0 = \frac{1}{k_0}\sqrt{\frac{\epsilon_0}{\mu_0}}\boldsymbol{k} \times \boldsymbol{E}_0 \tag{3.7}$$

and

$$\boldsymbol{E}_0 = -\frac{1}{k_0 n^2}\sqrt{\frac{\mu_0}{\epsilon_0}}\boldsymbol{k} \times \boldsymbol{H}_0. \tag{3.8}$$

Equations (3.5)–(3.8) define a complex representation of a plane electromagnetic wave.

3.1.1 Angular spectrum representation

Since a plane wave is a solution of Maxwell's equation, also any superposition of plane waves is a solution due to the linearity of Maxwell's equations. Further, Fourier analysis suggests that any electromagnetic wave can be represented as a weighted superposition of plane waves.

Let the x component of the electric field vector to be denoted as $E_x(x, y, z)$, assume that the field is known at plane $z = z_0$ and there are no sources in the positive half-space $z > z_0$. Now, it straightforwardly follows from solving the x component of Helmholtz equation (3.2) with the use of Fourier analysis that

$$E_x(x, y, z) = \iint_{-\infty}^{\infty} A_x(k_x, k_y) \exp[\mathrm{i}(k_x x + k_y y + k_z \Delta z)] \, \mathrm{d}k_x \mathrm{d}k_y, \tag{3.9}$$

where $\mathbf{k} = (k_x, k_y, k_z)$ is wave vector, $\Delta z = z - z_0$, and k_z is defined as

$$k_z = \begin{cases} \sqrt{k^2 - k_x^2 - k_y^2}, & \text{if } k_x^2 + k_y^2 \leq k^2 \\ \mathrm{i}\sqrt{k_x^2 + k_y^2 - k^2}, & \text{if } k_x^2 + k_y^2 > k^2 \end{cases}. \tag{3.10}$$

Fourier inversion at the plane $z = z_0$ leads to an expression for $A_x(k_x, k_y)$, where $E_x(x, y, z_0)$ is the field at the plane $z = z_0$:

$$A_x(k_x, k_y) = \frac{1}{(2\pi)^2} \iint_{-\infty}^{\infty} E_x(x, y, z_0) \exp[-\mathrm{i}(k_x x + k_y y)] \, \mathrm{d}x \mathrm{d}y. \tag{3.11}$$

The equations (3.9)–(3.11) describe the angular spectrum representation where the expression $A_x(k_x, k_y)$ is the angular spectrum.

3.2 ENERGY QUANTITIES AND POLARIZATION

Due to high frequencies in the optical region, it is only possible to detect time averages over multiple oscillations. The time averaged electric energy density can be written as

$$\langle w_\mathrm{e}(\boldsymbol{r}, t) \rangle = \frac{1}{4} \varepsilon \varepsilon_0 |\boldsymbol{E}(\boldsymbol{r})|^2, \tag{3.12}$$

where ε denotes the electric permittivity of a material and ε_0 permittivity of vacuum [52]. Respectively, the time averaged magnetic energy density is written as

$$\langle w_{\mathrm{m}}(\boldsymbol{r},t)\rangle = \frac{1}{4}\mu_0|\boldsymbol{H}(\boldsymbol{r})|^2, \tag{3.13}$$

where μ_0 is the magnetic permeability of vacuum [52]. The total time averaged energy density is the sum of the electric and magnetic energy densities

$$\langle w_{\mathrm{total}}\rangle = \langle w_{\mathrm{e}}\rangle + \langle w_{\mathrm{m}}\rangle. \tag{3.14}$$

The time-average of Poynting vector is written as

$$\langle \boldsymbol{S}(\boldsymbol{r},t)\rangle = \frac{1}{2}\Re\{\boldsymbol{E}(\boldsymbol{r}) \times \boldsymbol{H}^*(\boldsymbol{r})\}, \tag{3.15}$$

where the asterisk denotes a complex conjugate.

Polarization of light is described by the orientation of its electric and magnetic field components. Throughout this thesis linear polarization is denoted by notations TE (transverse electric component), which by definition has electric field being perpendicular to the plane of incidence, and TM (transverse magnetic component), which is respectively characterized by its magnetic field being perpendicular to the plane of incidence.

3.3 GRATING DIFFRACTION

A well known grating equation [53] describes the light diffraction from a structure modulated by a period d as

$$n_1 \sin\theta_i = n_2 \sin\theta_m + m\lambda/d, \tag{3.16}$$

where λ is the wavelength, n_1 and n_2 are the refractive indices of the incident and transmitted layers, $m = 0, \pm 1, \pm 2...$ is the number of a diffracted order with corresponding propagation angle θ_m, and θ_i is the propagation direction of the incident wave.

Here we restrict to examine one-dimensionally periodic permittivity of the grating that can be expressed in the form

$$\hat{\varepsilon}(x+d,z) = \hat{\varepsilon}(x,z), \tag{3.17}$$

where d defines the period of the structure along x direction.

If we then assume that the input field is a plane wave in xz plane that propagates in the direction defined by wave vector $\boldsymbol{k}$. Now, the expression for the wave vector can be given as

$$\boldsymbol{k} = k_x \hat{\mathbf{u}}_x + k_z \hat{\mathbf{u}}_z, \tag{3.18}$$

where k_x and k_z are components of the wave vector and $\hat{\mathbf{u}}_i$ denotes the direction. Now, the use of the well known Bloch-Floquet's theorem and boundary conditions leads to the fact that both the output field and the field inside the grating must be pseudoperiodic [54]:

$$E(x+d,z) = E(x,z)\exp(\mathrm{i}k_x d) \tag{3.19}$$

3.3.1 Fourier modal method

In general, for solving the computational problems in micro- and nanophotonics, there are two kinds of commonly used approaches that are based on solving Maxwell's equations either in the space-time domain or in the spatial frequency domain. In the space domain the Maxwell's equations are represented as partial differential equations that are solved numerically through spatial sampling points [55]. The most common methods employed are the Finite-difference time-domain (FDTD) [56, 57] and Finite element method (FEM) [58].

On the other hand, in the spatial frequency domain the solving of Maxwell's equations is based on their algebraic forms. The electromagnetic field can be represented by a Bloch eigenmode expansion which particularly in Fourier-modal method (FMM) is represented by pseudo-Fourier series [59].

A standard analytical algorithm used commonly together with FMM is S-matrix method which provides necessary information of

scattering properties of the structure with a high numerical stability [60,61]. An electromagnetic field is represented by a superposition of positive and negative Bloch eigenmodes with coupling coefficients that are specific for each mode. Positive modes represent forward propagating modes and pure evanescent modes whereas the negative modes represent respectively backward propagating modes. The analysis is carried out in a such way that the boundary conditions at the edges of the materials are satisfied.

If a structure, to be simulated, is not periodic or a non-plane wave illumination is used, it is possible to create periodical computational units with a period that is wide enough to rule out the periodic effect from the neighboring unit. Similarly a likely situation is that the computational unit size has to be restricted in order to analyze it by reasonable calculation capacity and to avoid the cross-talk from neighboring units due to the periodical nature of the FMM. Then it is possible to employ a perfectly matched layer (PML) between the computational units [62,63]. The PML acts as an artificial infinite half-space between the units while the properties of the eigenmodes are preserved.

A more detailed approach to FMM can be found in the references [59,61,64,65].

3.4 RESONANCE WAVEGUIDE GRATING

The phenomena that occur in a resonance waveguide grating (RWG), which is often referred also as a guided-mode resonance filter or a leaky-mode resonance filter, originates in Wood's observations of resonance anomalies in 1902 [66]. Wood's study was replenished by Hessel and Oliner who presented a theoretical reliance for two different types of variations in 1965 [67]: Rayleigh wavelength type and resonant type. The phenomena were first explained for coated dielectric gratings by Mashev *et al*. [68] in the late 80s. Since then they have been comprehensively studied by Magnusson and Wang [69,70] and others [71]. Several applications have been proposed for such devices, covering a wide range of areas from spec-

tral filtering [72,73] to biosensors [35,74,75], and second harmonic generation [76,77].

The resonance phenomena rely on the evanescent modes created by a surface modulation that interfere either constructively or destructively together with the propagating mode. Due to subwavelength modulation, the 0th order mode is the only propagating mode and any other mode exists in an evanescent form. In this chapter we review the properties of the RWG in some detail.

In this work, the resonance waveguide grating concept has been employed in Papers **I–III**. In Paper **I**, the RWG is used to increase fluorescence detection sensitivity in case of laser induced excitation and in Paper **II** the same concept is used for fluorescence detection enhancement with broad band and wide angle excitation. Further, in Paper **III**, the RWG is combined with a surface enhanced Raman scattering (SERS) substrate to increase Raman signal detection from a nanochannel formed between the two devices.

3.4.1 Properties

In the simplest case, illustrated in Fig. 3.1, the RWG consists of a grating layer with subwavelength modulation where d is a period of the modulation and $n_2(x)$ is the refractive index distribution of the modulated layer along x direction. Here we have defined the effective refractive index as

$$n_{\text{eff}} = \int_0^d n_2(x)\, \mathrm{d}x, \tag{3.20}$$

which needs to be higher than the neighboring indices for coupling of a RWG mode.

In the resonance condition the incident wave couples into the effective high index layer. This has a strong analogy to the conventional waveguide coupler. Due to the interference, also the local field intensity is greatly affected and significantly strong intensity hot spots appear in the guided-mode layer. However, the reciprocity requires the field to be coupled out from the waveguide mode and this is to the direction of the reflection. Therefore, in

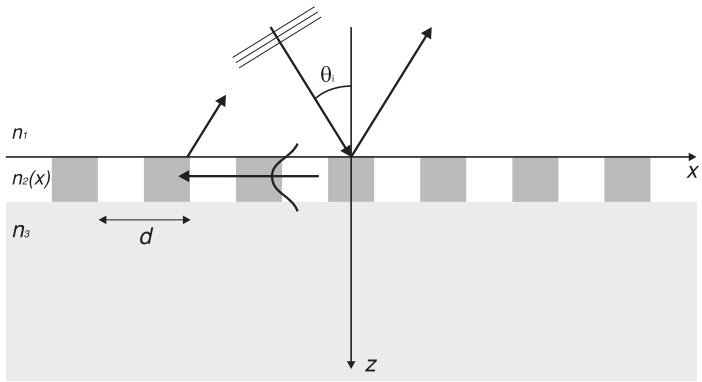

Figure 3.1: Schematic diagram of a resonance waveguide grating. θ_i denotes the angle of incidence, n_i are the refractive indices of each layer and d is the period of the grating. The arrow along the modulated layer illustrates the RWG mode propagation which is, after propagating a short distance, scattered out to the direction of the reflection.

the complete resonance condition a strong change in reflection efficiency is observed as a function of wavelength or incident angle, for instance.

Examination of a plane wave illumination into a RWG structure with the geometry shown in Fig. 3.2 leads to observation of rapid changes in reflection efficiency. Figure 3.3 shows the changes in the reflection efficiency as a function of wavelength for TM and TE polarized modes where the peaks correspond the coupling of different modes. The choice of the incident light polarization is crucial as the polarization affects the guided mode propagation constant. The parameters used for the calculations are as follows: the angle of incidence in air is 8°, modulation period is 225 nm, modulation fill factor is 0.35, modulation height in SiO_2 substrate ($n_3 = 1.46$) is 150 nm and the high index TiO_2 film ($n_g = 2.47$) thickness is 40 nm.

3.4.2 Functionality

The greatest interests in a resonant waveguide grating functionality in Papers **I–III** is the ability to control the local field intensity inside the structure and its near field, as well as the beaming effect due to

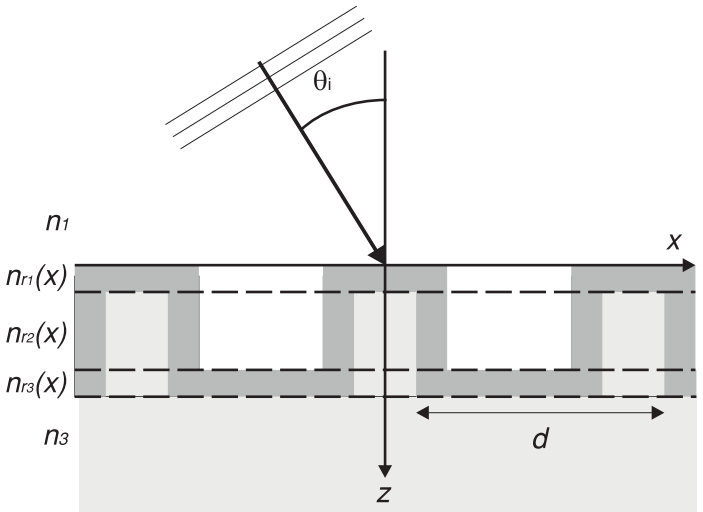

Figure 3.2: Schematic diagram of a cross-section of a high refractive index thin film coated resonance waveguide grating. A dielectric substrate, periodically modulated with a period d, is coated with a high refractive index thin film.

out-coupling of guided mode.

A particular design of a RWG used in Papers **I–III** is shown schematically in Fig. 3.2. The configuration involves either a modulated glass or polymer substrate which is coated with a thin film

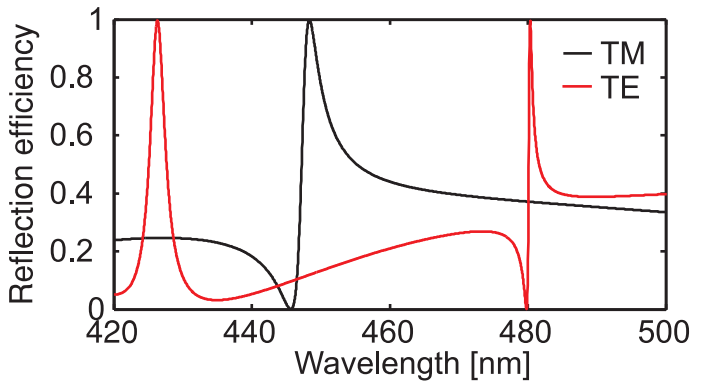

Figure 3.3: An example on rapid changes in reflection efficiency as a function of incident wavelength.

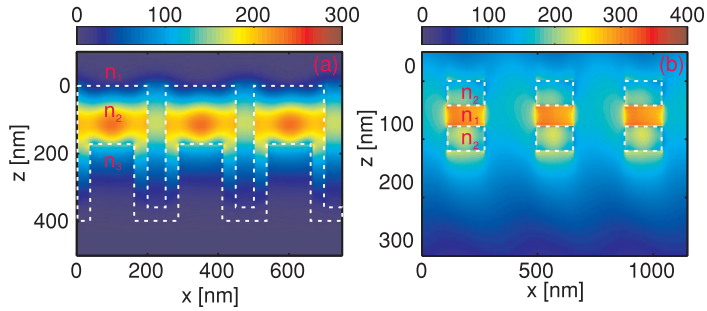

Figure 3.4: (a) The time average electric energy density in a thin film RWG, where maximum of incident field is scaled to unity and $n_2 > n_1, n_3$. (b) A free standing RWG configuration is used to create the hot spot outside of high index material.

of high refractive index TiO_2. Depending on a deposition method of the TiO_2 layer, the refractive index and the ratio between the top, bottom and sidewall thicknesses vary. In the grating layer refractive indices are described by $n_{ri}(x)$ which define periodically changing index a layer by layer.

For the purposes of enhancing excitation in fluorescence or Raman detection, it is essential to control the field distribution in the locations where the detectable molecules appear. It is no longer adequate to just examine reflection efficiency to choose the correct parameters but the field distribution should be calculated. As far as any invariance or certain symmetries appear in the structures, the computational cost is reasonable. In Papers **I–III** invariance in y direction is assumed.

Figure 3.4 shows that depending on the choice of materials and structure parameters, a RWG may carry a guided mode and respectively the local high energy hot spots may appear either inside the grating layer 3.4(a) or in the near field outside it 3.4(b). The latter example has an analogy to slotwaveguide structures [32] but the waveguide mode propagation is limited as described earlier in this chapter. In this example, Si_3N_4 is used as a high refractive index material which is surrounded by water.

3.5 LIGHT AND MATTER INTERACTION

In this section, a brief background for the the most essential light-matter interaction processes applied in this work are described.

3.5.1 Fluorescence emission and Raman scattering

Fluorescence of molecules or artificial materials such as quantum dots arises from the radiative relaxation of an excited molecule. The Jablonski's diagram, in Fig. 3.5, describes the process where a molecule absorbs an exciting photon with the energy higher than the gap energy between the ground state and the excited states. Further, non-radiative relaxation mechanisms occur until the radiative relaxation takes place from the lowest excited state back to the ground state. The wavelength of the radiative relaxation is usually longer than the wavelength of an excited photon due to the energy losses in the non-radiative processes. If additional energy is apparent in the process, such as two-photon excitation, a change to the higher energy radiation is also possible.

Raman scattering, discovered by C. V. Raman in 1928, is an inelastic scattering of a photon that arises from intra-molecular vibrations when excited with a photon energy lower than is required to excite the electrons from the ground state to the lowest excited

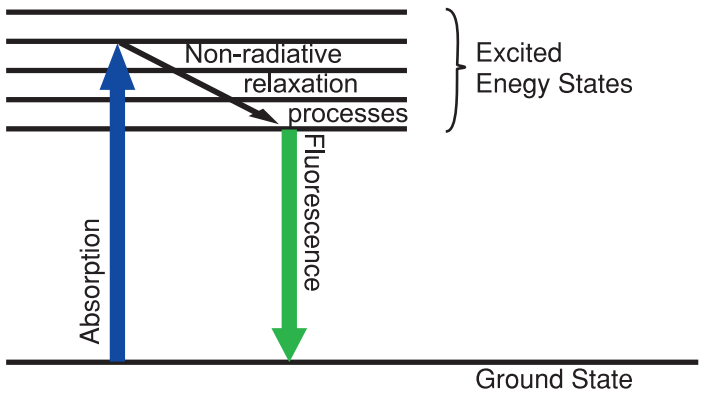

Figure 3.5: Fluorescence relaxation mechanism in the Jablonski diagram.

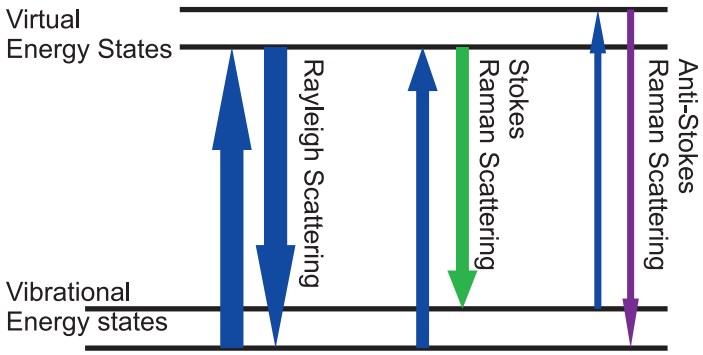

Figure 3.6: Schematic diagram of Rayleigh and Stokes scattering processes.

state. The diagram in Fig. 3.6 shows the processes for Raman and Rayleigh scattering. In Rayleigh scattering the scattering process is elastic and scattered photons have the same energy as the incident photons do. This is a far more common process than the Raman scattering that can take place in two different cases. During a scattering event a photon either loses some energy to the molecule or gains some energy from the molecule. The first event is called a Stokes shift and the latter an anti-Stokes shift in the frequency of the scattered photon.

3.5.2 Surface plasmons

Surface plasmon oscillations can take place at an interface between two materials, a metal and a dielectric normally. The oscillation originates from the excitation of conduction electrons near a metal surface. A propagating surface plasmon polariton is exited as a confined electromagnetic field when the incident light frequency matches the surface plasmon resonance frequency on the smooth metal-dielectric interface. However, direct illumination of a smooth metal surface does not excite surface plasmons but a momentum of the incident photon needs to be matched to the momentum of surface plasmon. This can be done, for instance, by prism coupling [78]. If such resonant oscillation is limited to a small volume such as a set of nanoparticles, it is known as a localized surface plasmon.

It is also possible to couple a plane incident wave into a surface plasmon mode by introducing a geometrical periodic modulation on the metal surface. The period may be chosen by the relation [79]

$$d = \frac{m2\pi}{\Re\{k_{\mathrm{sp}}\} - k_0 n \sin\theta}, \tag{3.21}$$

where θ is the angle of incidence, n is the refractive index of the dielectric, m is the index of the diffraction order, and k_{sp} is the propagation constant of the surface plasmon.

3.5.3 Surface enhanced Raman scattering

Raman scattering, by nature, is very weak as the probability of a Raman scattering event is roughly only 10^{-5} to 10^{-6}. In the late 1970s it was discovered that molecules adsorbed in a specially fabricated silver surface produced an unexpectedly high Raman signal [80]. Since then surface enhanced Raman scattering (SERS) has been developed into a highly effective tool in biological and chemical sensing [81–83].

It is known that SERS enhancement can be attained either by enhancing electromagnetic field intensity on a surface capable of exciting surface plasmon waves [84,85] or by electro-chemical properties of the material through a charge-transfer phenomenon [86,87].

3.5.4 Optically excited acoustic waves

In general, optically excited acoustic waves are generated when an incident light pulse is partially absorbed in a material. There are three commonly used approaches to evaluate high-frequency optoacoustics measurements in thin films [88].

Firstly, a short pulse of light, commonly in a pico- or femtosecond range, is used to mildly heat the film surface which creates a longitudinal acoustic pulse that propagates into the depth of the structure. The time dependence of reflection is measured by a variably delayed, low intensity, probe pulse. Reflection of acoustic waves appear from buried interfaces within a stack-like material.

The data can be used to determine longitudinal acoustic velocities or the film thicknesses, given that one of the parameters is known.

In the second approach a tightly focused excitation pulse generates surface acoustic waves. The propagation of the acoustic waves is monitored by a spatially displaced probe with a known separation distance. The typical data consists of the oscillation due to the band width of the excitation source as the created sound pulse velocity depends on the excitation wavelength.

The third method employs a spatially modulated excitation geometry which leads to launches of counter-propagating surface acoustic waves. Now, the probing gives information about surface acoustic modes and it is also possible to attain information of longitudinal modes in the case of thin film structures.

The spatial resolution is substantially limited by the acoustic wavelength and excitation spot size [89]. Optical masking of a sample may be used to control the excited area and excitation efficiency [90,91]. In this work, in section 6.2, the spatial sub-wavelength modulation is generated by an integrated resonance waveguide grating.

4 Fabrication methods

This chapter gives an overview of the most relevant fabrication processes used in this work. As the work mainly takes advantage of the fabrication processes developed earlier, only a decent background for the processes used is given here. There is a rather substantial assortment of references in each section for a deeper insight to the processes and a quite comprehensive overview of the field is given in Ref. [92].

In order to give an idea about a typical fabrication process, Fig. 4.1 shows an example of process steps used to fabricate a resonant waveguide grating. Here a glass substrate is coated with a metal film followed by a spin coated electron beam resist. The resist is patterned with electron beam lithography (a) and is further used as a mask to etch the features down to the metal layer (b). Now, the metal masking is used to transfer the modulation to the glass substrate in another etching process (c). Residues of either masks are removed (d) and, finally, a high refractive index material is coated on the modulated substrate.

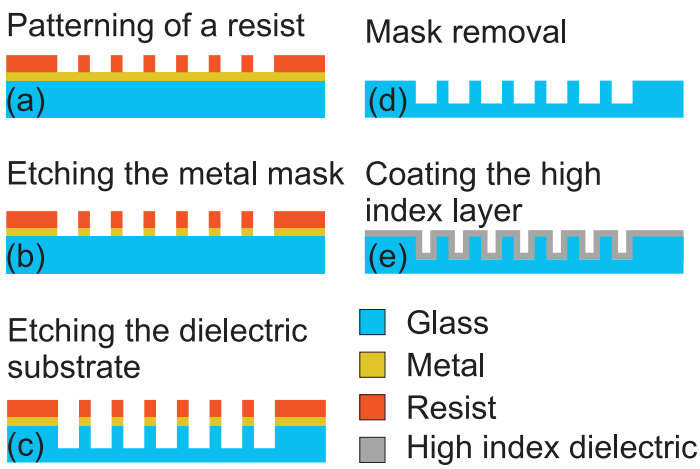

Figure 4.1: A possible process flow to fabricate a RWG.

4.1 ELECTRON BEAM LITHOGRAPHY

The electron beam lithography technology has emerged from the field of microelectronics as an important tool to manufacture components for photonics needs. In theory, the resolution of a high end electron beam lithography tool is around five nanometers but the resolution is also affected by other process steps and used materials. Several techniques are reported in the literature to achieve controlled feature sizes below 10 nm by using either direct write [49,93] or more complex techniques [25,48].

Vistec EBPG5000+ES HR electron beam lithography tool was used in this work.

4.1.1 Resist technology

Electron beam resists can be roughly divided into two categories depending on their dissolving properties. If an exposed resist dissolves during a developing process the resist is called positive. Vice versa, it is called negative when unexposed resist dissolves.

The positive resists used in this work are Polymethyl methacrylate (PMMA) and ZEP 7000-22, which is a styrene/chloromethyl acrylate copolymer dissolved in digmyne (bis(2-methoxyethyl)ether). The first is commonly provided by several producers and the latter is produced by Zeon Corporation. Both resists are relatively stable against storing and have sufficiently good resolution, down to approximately 50 nm at the room temperature with ZEP 7000-22. However, a resolution close to 10 nm is demonstrated with cold developement [94].

Hydrogen silsesquioxane (HSQ) was used as a negative resist. It has significantly higher resolution and features down to sub-10 nm are reported [49]. However, stability over time is an issue with HSQ and careful monitoring of current quality is critical.

4.2 THIN FILM DEPOSITION PROCESSES

This section describes shortly the thin film coating techniques used in this work. Both oxide and metal films were deposited, using mainly thermal evaporation and atomic layer deposition. The optical properties of a thin film depend strongly on the deposition technique used [95].

4.2.1 Evaporation

The evaporation of a source material can be done by applying electric current through the material or alternatively the heating is done by an electron beam. In either case, a high vacuum environment, usually in the range of 10^{-5} to 10^{-7} mbar, is required to avoid reactions between vapor and atmosphere and thus resulting in a solid film quality. In this work, the thermal evaporation was used to coat both oxide and metal films. By the nature of the process, the films are commonly rather porous. In some cases, the porosity may be decreased by adding external energy such as heating a sample [96]. The main evaporation tool used in the work was Leybold L560, but also Kurt J. Lesker Lab-18 evaporation unit was used.

4.2.2 Atomic layer deposition

Atomic layer deposition (ALD) provides a possibility to fabricate several type of materials with high accuracy [97, 98]. In principle, an ALD process cycle consists of pulses of precursors separated by an inert gas purge. This results in the growth of a material almost ideally, an atomic layer by atomic layer.

In this work, Beneq ALD TFS 200 unit was employed with thermal and plasma options to coat high refractive index TiO_2 films for resonance waveguide gratings, to fabricate TiO_2 and SiO_2 etching masks for aluminium etching, as well as to adjust surface adhesion properties with Al_2O_3.

4.3 REPLICATION

Nanoimprint lithography (NIL) and hot embossing replication have been used for quite a while as high resolution replication processes of nanostructures [99–101]. Currently they are emerging in commercial roll-to-roll [102] manufacturing of micro- and nanostructures. In the latter, a combination of heat and pressure is used to transfer modulation from a mold to a substrate. This is a fast and cost efficient method to replicate nanopatterns to polymers such as polycarbonate (PC) or cyclo-olefin copolymer (COC). In the NIL replication the modulation is transferred to the UV-curable NIL-resist and a pattern can be further processed down to the underlying material, for example with an etching process. Obducat NIL Eitre 3 was used for the NIL and hotembossing in this work.

4.4 DRY ETCHING

Dry etching processes can be broadly divided into physical and chemical ones. In the physical process the surface to be etched is bombarded by heavy atoms such as Argon atoms in order to remove some material from the surface. In chemical etching, molecular interactions take place in the plasma generated in the etching chamber. However, rarely an etch process is strictly only chemical or physical but commonly both aspects are involved.

The areas that are not wanted to be removed are covered by an etching mask which can simply be a resist layer or often some more resistant material against the etching process. The chemical etching processes are often highly isotropic and different compositions of chemical and physical processes may be required to achieve desired features. Usually, the higher anisotropy requires also the use of sidewall passivation which can be done, for example, by adding O_2 gas in aluminium process or more commonly by creating a passivation polymer as a reagent product.

4.4.1 Oxide masking in Aluminium etching

The etching of aluminum films requires special care due to rapid oxidation through a thin, thermally evaporated, aluminium film. ALD fabricated TiO_2 and SiO_2 films provide reasonable protection against the oxidation, serving at the same time as an etch mask for aluminium etching. Unwanted oxidation strongly affects etching properties of the film, as well as the properties of a final device, particularly if the aim is to employ the surface plasmons.

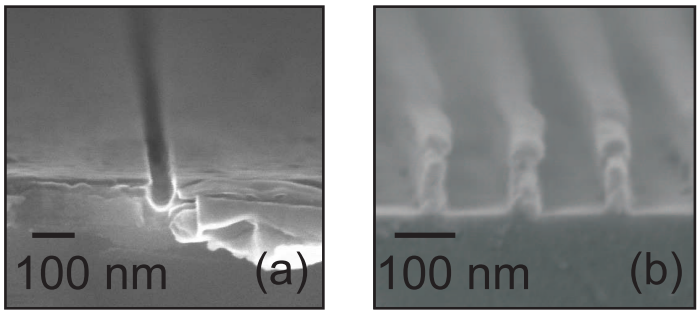

Figure 4.2: Scanning electron microscope images of (a) 50 nm slot and (b) 50 nm lines etched in Al film.

The aluminium etching, using BCl_3 and Cl_2 gases, is highly selective against oxides and therefore it is possible to work with a very thin oxide mask ($\sim$ 10 nm). The thin mask enables the etching with high resolution features as the scanning electron microscope image shows in Fig. 4.2(a). Here a 50 nm wide slot is etched down to aluminium that is masked with a 10 nm layer of TiO_2. In Fig. 4.2(b) 50 nm lines are etched in a similarly prepared aluminum film.

A drawback in some cases may be that the mask, especially a TiO_2 film, may be difficult or impossible to remove from the aluminum surface after etching. However, the layer is often thin enough to be included in the design itself without a significant disturbance.

4.5 TEMPLATE STRIPPING

It is almost unavoidable that the uppermost surface of a thin metal film fabricated by standard coating tools remains rather rough. This distinctly affects the applications where the control of light scattering from a surface has a high importance. However, it has been shown that by stripping an evaporated metal thin film from a smooth surface results in atomic scale smoothness of the metal surface [103, 104].

In Paper **IV** this method is employed for aluminum thin films. To adjust the adhesion properties a few nanometers of Al_2O_3 was deposited on a Si (100) wafer with the ALD process. Further, the aluminum was deposited on the adhesion controlled Si wafer using a thermal evaporation process. After pattering the uppermost

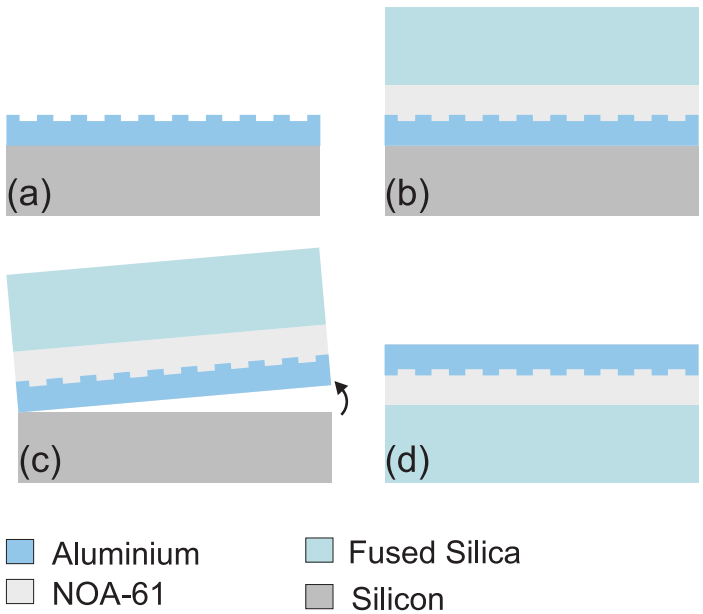

Figure 4.3: The template stripping process flow. A modulated aluminum film on a Si substrate (a) is attached with an UV curable glue (NOA-61) to a glass substrate(b). N_2 pressure is applied to detach the aluminum film from the Si wafer (c) resulting in a very smooth aluminum surface (d).

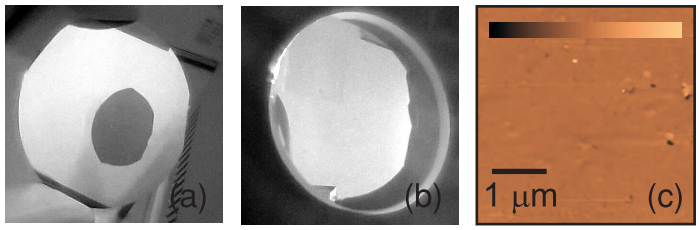

Figure 4.4: Template stripping process where the film is removed from the original Si wafer (a) and glued on the new SiO_2 sample (b). An atomic force microscope image of the stripped surface (c), the color bar refers the scale -10 to 10 nm.

surface the stack was glued on a SiO_2 wafer with an UV-curable NOA-61 (Northland Optics) glue as shown in Fig. 4.3. UV exposure was used to harden the glue and the initial Si wafer was then removed by applying pressurized N_2 flow through the intersection. Figures 4.4(a) and 4.4(b) show the stripping from a Si wafer to a SiO_2 substrate.

For the transfer of a sub-micron modulation from one substrate to another, the solvent and heat assisted immersion [105] of the NOA-61 was performed to ensure the glue penetration down to the bottom of the modulation. Here, a drop of a low viscosity solvent (acetone) is applied on the modulated area followed by a drop of NOA-61. The aluminum film on a Si wafer is heated up to 80°, which evaporates the acetone from the sample allowing the glue with decreasing viscosity to flow into the grooves.

This method was demonstrated to result in a sub-nanometer rms surface roughness over the area of 3 μm^2 despite of some higher scale impurities visible in Fig. 4.4(c). In addition, a uniform glue-metal interface was achieved due to high accuracy glue penetration into 180 nm wide grooves.

4.6 DISCUSSION

A brief glance through the micro- and nanofabrication processes used in this work was given in this chapter. Even though most of the processes were already developed earlier in a general level, it

is evident that any full process flow to realize a device, containing highly controlled nanoscale features, requires careful tuning.

Choices of fabrication methods and materials greatly affect the overall process behavior and thus also the final product. This has to be taken account in design and fabrication. For example, by choosing an ALD process instead of electron beam evaporation the refractive index of $Ti0_2$ changes approximately from 2.15 to 2.45. Even small changes within one process may lead to a result far from optimal in another process followed the first one. A slight change in vacuum level in Al evaporation, for instance, may result in complete inoperativeness in the etching process.

5 Applications to fluorescence imaging

The applications presented in this chapter are originally published in Papers **I** and **II**. Both approaches are based on the resonance waveguide grating (RWG) concept described in section 3.4. In addition, a numerical model for electric dipole emission scattering in the immediate neighborhood of a RWG is discussed.

5.1 ENHANCED SENSITIVITY IN LASER INDUCED FLUORESCENCE

Due to the properties presented earlier in section 3.4.2, the highly confined excitation energy can be used to enhance the excitation of the fluorescent species in the near-field of a RWG. The enhanced excitation together with the enhanced directionality of fluorescence, that arises from the emission coupling into the waveguide mode of the device, makes the RWG concept highly attractive in fluorescence detection.

We have shown, in Paper **I**, that the presence of a RWG in laser induced fluorescence results in a 530-fold increase in fluorescence signal which is detected within a narrow directional emission cone. The enhancement was demonstrated by using enhanced green fluorescent proteins (EGFP) as fluorescent molecules. It was also approximated, following the approach from Refs. [106, 107], that the fluorescence signal emitted towards the beaming angles has an increased spatial coherence length of 15 μm. This follows from the emission coupling and propagation in the waveguide mode of the grating.

The technique can be used similarly in total internal reflection microscopy based imaging techniques [108, 109] and it is capable of

living cell detection [35].

5.2 BROADBAND EXCITATION TO OVERCOME ANGULAR SENSITIVITY OF RWG

It was stated earlier that a resonance waveguide grating is highly sensitive to the angle of incidence. However, a common practice in conventional microscopy is to illuminate and detect a sample through an objective, in which case the illumination is not directional. In Paper **II**, we have shown that by simply replacing a monochromatic excitation source by a broad band source, the RWG-based measurement system can be used to greatly enhance fluorescence detection in the conventional epifluorescence microscope.

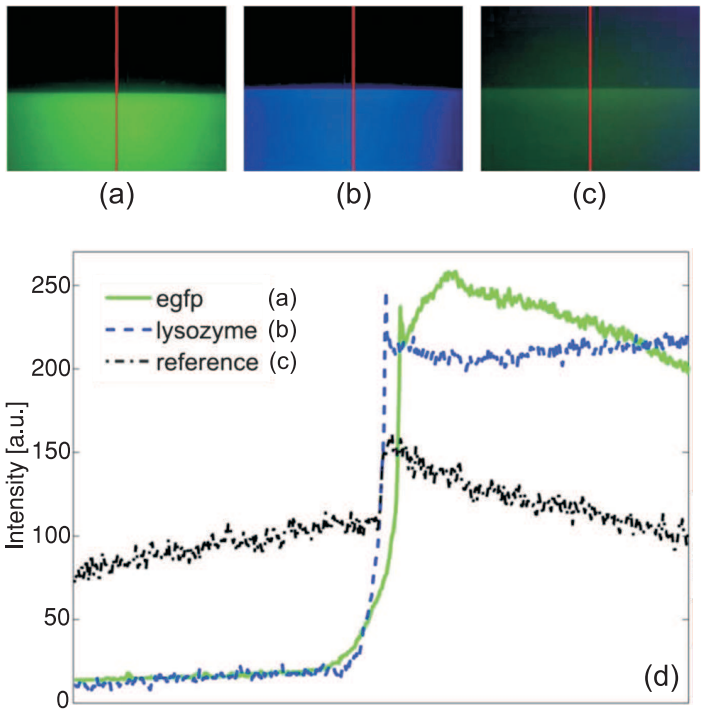

Figure 5.1: Fluorescence microscope images of fluorescent emission from the interfaces of RWGs (bottom) and planar (top) surfaces (a–c) and the corresponding intensity distribution plots along red lines (d).

We have demonstrated about 30-fold enhancement in the arc-discharge mercury lamp (HBO) excited fluorescence signal compared with the one measured on a flat surface. The excitation bandwidth of 450–490 nm was used. The enhancement was demonstrated with EGFP and lysozyme proteins, the latter of which have natively very low fluorescence and the results show that the method is promising also for label-free detection.

Fluorescent microscope images in Figs. 5.1(a) and 5.1(b) show improved fluorescence signal of EGFP and Lysozyme respectively. Figure 5.1(c) shows a reference image where the surface modulation parameters are chosen a such way that a RWG functionality is not exploited. This shows that changed geometry does not play a significant role in the enhancement process. The intensity distributions along red lines in Figs. 5.1(a)–5.1(c) are plotted in Fig. 5.1(d).

5.3 THE EFFECT OF RWG ON SCATTERING PROPERTIES OF AN ELECTRIC DIPOLE

If the fluorescence emitting molecules or particles are assumed to have a size much less than the RWG period, these emitters can be treated as electric dipoles. By employing the FMM and the angular spectrum representation for the dipole radiation, the emission coupling into the RWG mode can be analyzed in detail.

The angular spectrum of light emitted by an arbitrarily aligned dipole with monochromatic radiation can be defined by starting from a vector potential description of a dipole [110]

$$\mathbf{a}(\mathbf{r}) = \mathrm{i}k\mathbf{p}U(r), \tag{5.1}$$

where $k = k_0 n$, $\mathbf{p} = (p_x, p_y, p_z)$ is the dipole moment, and $U(r) = \exp(\mathrm{i}kr)/r$ with $r = \sqrt{x^2 + y^2 + z^2}$. A straightforward calculation leads to the following relations for the electric $\mathbf{e}$ and magnetic $\mathbf{h}$ components of the angular spectrum representation:

$$\mathbf{h}_{\mathrm{TE}}(k_x) = \frac{\mathrm{i}k}{2\pi\mu_0} p_y \left(-\hat{\mathbf{x}} + \frac{k_x}{k_z}\, \hat{\mathbf{z}} \right) \tag{5.2}$$

$$\mathbf{e}_{\mathrm{TE}}(k_x) = \frac{1}{2\pi}\frac{k^2}{k_z} p_y \, \hat{\mathbf{y}} \tag{5.3}$$

$$\mathbf{h}_{\mathrm{TM}}(k_x) = \frac{\mathrm{i}k}{2\pi\mu_0}\left(p_x - \frac{k_x}{k_z}p_z\right)\hat{\mathbf{y}} \tag{5.4}$$

$$\mathbf{e}_{\mathrm{TM}}(k_x) = \frac{1}{2\pi}\left(k_z p_x - k_x p_z\right)\hat{\mathbf{x}} - \frac{k_x}{2\pi}\left(p_x - \frac{k_x}{k_z}p_z\right)\hat{\mathbf{z}}. \tag{5.5}$$

In the equations (5.2)– (5.5), μ_0 refers for the magnetic permeability of vacuum, $\hat{\mathbf{x}}, \hat{\mathbf{y}}$, and $\hat{\mathbf{z}}$ are unit vectors, and k_x, k_z are components of the wave vector.

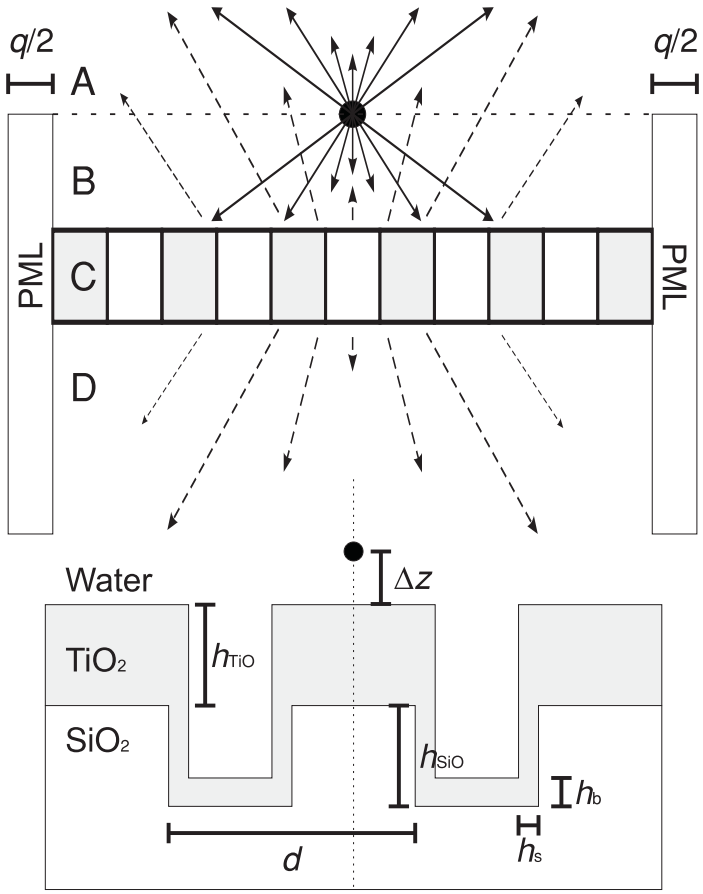

Figure 5.2: An illustration of the computational concept.

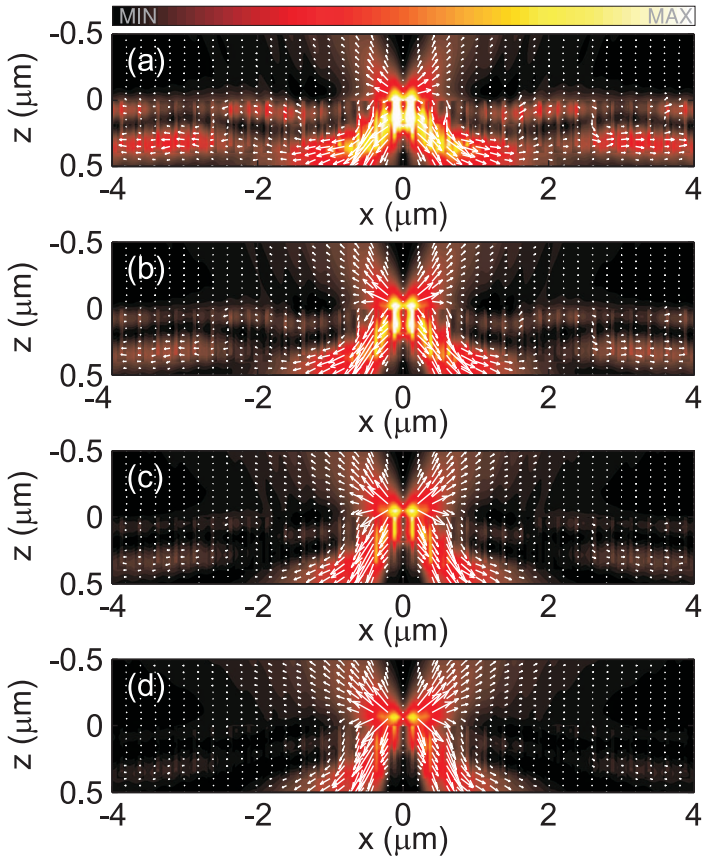

Figure 5.3: The time averaged electric energy density (color scale) and Poynting vectors (arrows) show light coupling from a single dipole, oriented along z axis, into the RWG mode when the dipole distance from the surface is (a) 10 nm, (b) 30 nm, (c) 50 nm, and (d) 70 nm.

The computational concept is shown in Fig. 5.2. Here, the geometry is divided into four part as illustrated with the capitals **A**–**D**. The area **A** includes backward scattered emission from the RWG and the part of dipole emission that has direction of propagation outward from the RWG. The dipole emission propagating towards the grating is handled in the area **B** together with reflected emission from the grating. The field inside the RWG structure and the transmitted field are considered in the areas **C** and **D**, respectively.

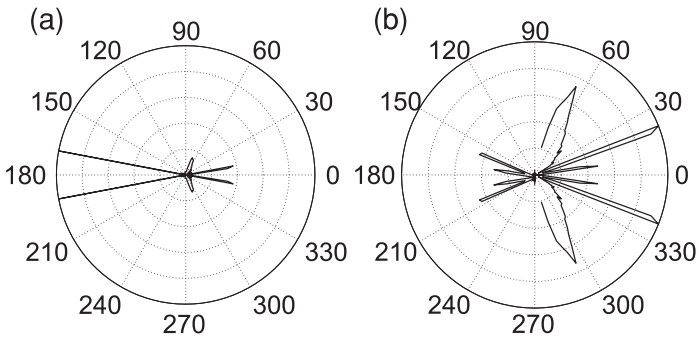

Figure 5.4: The angular far field intensity distributions of a single dipole radiating on the RWG at the wavelength of 509 nm (a) and at a gaussian weighted wavelength band of 509 ± 20 *nm (b). The peak intensities are scaled to unity.*

A super period $D = 14.5$ μm consists of modulation with a period $d = 250$ nm and a perfectly matched layer $q = 4$ μm. The SiO_2 substrate ($n = 1.46$) has the fill factor $f = 0.5$ and the modulation depth $h_{\mathrm{SiO}} = 215$ nm. The high index TiO_2 layer ($n = 2.15$) has thicknesses of $h_{\mathrm{TiO}} = 175$ nm on the top, $h_{\mathrm{TiO}} = 39$ nm on the side walls, and $h_{\mathrm{b}} = 49$ nm on the bottom of the groove.

Figure 5.3 shows dipole emission, with wavelength of 509 nm, coupling into the RWG mode when the dipole distance Δz from the grating surface is varied, being (a) 10 nm, (b) 30 nm, (c) 50 nm, and (d) 70 nm. The dipole is placed at $x = 0$ position which corresponds the placement at center of a grating tooth. It is clearly visible that the coupling is extremely sensitive to the separation distance due to exponential attenuation of evanescent field and the effective coupling is lost within the distance less than a hundred nanometers.

The conditions, identical to the configuration shown in Fig. 5.3, yield highly directional far field intensity distributions plotted in Fig. 5.4(a) for a single wavelength of 509 nm and in Fig 5.4(b) for Gaussian weighted wavelength band of 509 ± 20 nm, which is a more realistic case for a fluorescent emitting molecule. Both cases show significantly narrow emission lobes propagating towards the half spaces on either side of the structure. Since resonance condition

is highly sensitive to the wavelength, in the broad band case the diffraction cones are broader and there are more possible diffraction angles.

5.4 DISCUSSION

We have shown that the resonance waveguide gratings provide an efficient method to enhance fluorescence detection. The method can be employed straightforwardly, without any modification in the imaging system, in conventional fluorescence microscopy.

The platform can be transferred to large scale production, using cost-efficient materials and manufacturing processes such as polymers and roll-to-roll fabrication combined with atomic layer deposition.

An interesting approach is to integrate the RWG concept within other photonic devices, leading to lab-on-chip type applications as the high performance in enhancing the fluorescence detection becomes crucial in miniaturized devices for low sample volumes and concentrations. A few examples are shown in the following chapter.

Simulations shown in this chapter predict that fluorescent emitting molecules have to be placed very close to the RWG surface to achieve efficient coupling of emission into a RWG mode. However, these simulation lack the possibility to place a dipole inside the grating groove where coupling, intuitively, might be even more efficient.

6 Horizontal slot waveguide channel

Two different applications to control the electromagnetic field interaction in systems consisting of a RWG and a functional metallic surface are presented in this chapter. The first application demonstrates a strong gain in a Raman signal from a nanometer scale horizontal slot waveguide channel and the latter predicts a method for high resolution excitation of acoustic surface waves in metallic thin films. Both applications take advantage of a proximity effect of the two surfaces.

6.1 ENHANCED RAMAN SIGNAL FROM NANOCHANNELS

In Paper **III**, we have shown an approximately 20-fold enhancement in Raman scattering measured from a sub-hundred nanometer slot channel formed by the RWG and SERS substrate, as shown in Figs. 6.1(a) and 6.1(b). The enhancement is demonstrated by comparison with a conventional SERS substrate within a corresponding slot arrangement. The enhancement of an electromagnetic field inside the presented slot has a close analogy with dielectric slot waveguides [32].

Figure 6.1(c) shows an average intensity of the Raman spectrum of rhodamine 6G for the reference configuration (black) and for the enhanced configuration when the sample is excited with TM (red) and TE (green) polarized light with the wavelength of 514 nm. Since SERS structure has randomly oriented particles, the reference signal is not affected by the choice between TM or TE polarization.

The system was initially optimized by looking for the maximum absorption of incident field into the system. The parameters from the initial optimization are used as a starting point for the search of a local field intensity maximum within the slot region, where the

detectable molecules appear.

Due to significant randomness of the SERS substrate silver particles in size and shape, rigorous modeling of the SERS substrate is not possible. To demonstrate the phenomena and approximate the best performing device parameters, a two-step-process for the design was launched. At first, a planar silver film was used instead of a SERS substrate and the grating parameters were first defined in this simplified configuration. After fixing the grating parameters

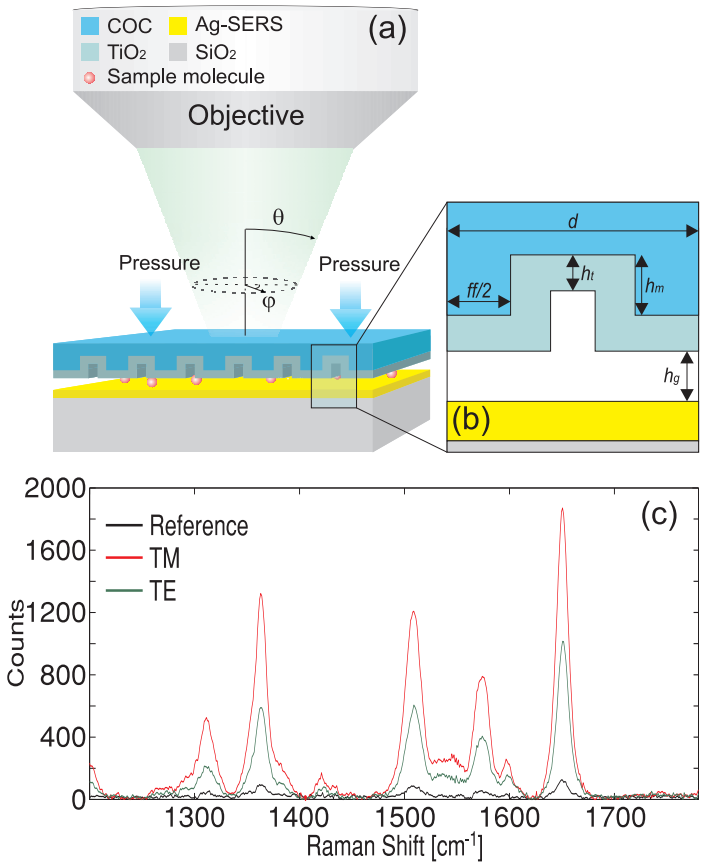

Figure 6.1: (a) An illustration of the horizontal slab waveguide configuration for Raman detection. (b) The close-up of the slot configuration.(c) The measured Raman signals of Rhodamine 6G from reference slot (black) and TM (red) and TE (green) excited signals from grating enhanced configuration.

a modulation on the silver film was introduced.

This approach shows that the system has two main benefits: The local surface plasmon resonance within a SERS substrate is greatly enhanced and also the field intensity within the slot region is enhanced. The first improves the SERS substrate performance and the latter enhances excitation within the slot volume, outside SERS hot spots, which predicts promising applications in nanofluidistics and on-line detection systems.

A common figure-of-merit for the SERS enhancement is the enhanecement factor (EF). It is most commonly defined [111] as

$$EF = \frac{I_{\mathrm{SERS}}/N_{\mathrm{Surf}}}{I_{\mathrm{RS}}/N_{\mathrm{Vol}}}, \tag{6.1}$$

where N_{Surf} and N_{Vol} are the average number of molecules in the interaction volume of the SERS and non-SERS measurement and I_{SERS} and I_{RS} are the Raman signals respectively. It may be challenging to measure the Raman signal on the non-SERS conditions and therefore it may be more convenient to compare the Raman and fluorescence signals of Rhodamine 6G that have the relation [112]

$$\frac{I_{\mathrm{IR}}}{I_{\mathrm{FL}}} = \frac{\sigma_{\mathrm{IR}}}{\sigma_{\mathrm{FL}}} = 10^{-9}, \tag{6.2}$$

where I_{FL}, I_{IR}, σ_{FL} and σ_{IR} are the fluorescence and Raman intensities and cross-sections respectively. Here, the intensity ratio follows from the cross-section ratio of normal Raman scattering and fluorescence. If the same number of molecules have an effect on both events, which can be justified by the sample handling techniques, the EF can be estimated as

$$EF = \frac{I_{\mathrm{SERS}}}{I_{\mathrm{FL}}}\, 10^{9}. \tag{6.3}$$

By using the figure-of-merit described in Eq. (6.3) the enhancement of $\sim 2 \times 10^9$ is achieved for the Raman signal from the advanced nanoslot configuration.

6.2 HIGH RESOLUTION ACOUSTIC SURFACE WAVE EXCITATION

A resonance waveguide grating can be used to effectively control

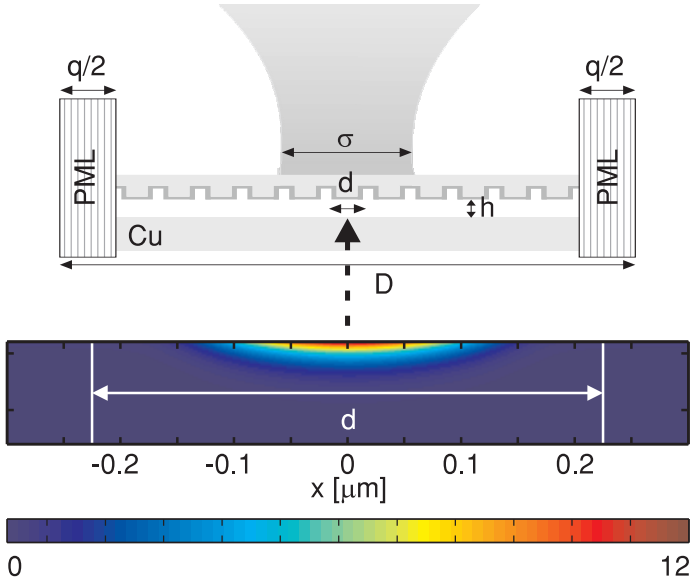

Figure 6.2: The concept of system and computational model on the top, and the time averaged energy density inside the Cu film on the bottom. A computational unit with a period D consists of periodical modulation with a period d and the perfectly matched layer having a width q. The resonance waveguide grating has been separated from the Cu film with the distance h. The incident gaussian beam has full width of σ in the focus.

the excitation of acoustic waves. In principle, the RWG is designed to capture a remarkable fraction of the incident energy to the system presented in Fig. 6.2. This is simply done by optimizing the parameters for the minimum reflection from the system. Further, the parameters can be tailored in such a way that the absorption occurs in carefully chosen spots in a metal film. In lower part of Fig. 6.2 the time averaged energy density within a grating period inside a copper film is shown. Here a gaussian incident beam with the wavelength of 800 nm and a focal width of 10 μm is applied. The maximum of the incident field is scaled to unity.

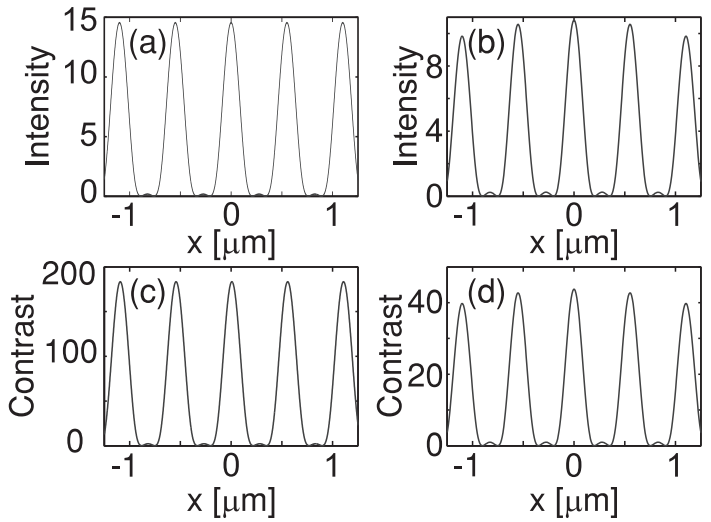

Figure 6.3: The intensity modulation on the surface of the absorbing Cu layer for a plane wave illumination (a) and for the gaussian illumination (b). The corresponding contrast to the average of the low intensity area are shown in (c) and (d) respectively for plane wave and gaussian incident fields.

It is shown that the energy can be guided to the well confined hot spot within a single period. These spots can be sized roughly down to $\lambda/3$ diameter and they have a strong contrast against the surrounding area which are the key features to launch highly controlled acoustic surface waves for high resolution detection. In Fig. 6.3(a) the plot shows the calculated intensity right inside the Cu layer along x direction for a plane wave type illumination at the wavelength of 800 nm. The intensity is scaled to the maximum of incident field. Figure 6.3(c) gives the corresponding contrast to the cold spot which is defined by the averaging intensity below $1/e^2$ value. Respectively Figs. 6.3(b) and 6.3(d) give the intensity and contrast for the gaussian type illumination which show that benefit is not lost by focusing that is required experimentally.

The proposed method has potential applications in semiconductor wafer metrology where non-destructive and high resolution detection is required.

6.3 DISCUSSION

The methods presented in this chapter predict possible applications for highly sensitive and non-invasive measurement tools for Raman and optoacoustic systems.

The drawback to be overcome is the requirement of highly sensitive positioning of such devices within less than a few hundred nanometers. The current capabilities in the nanofabrication technology enable the transfer of these methods to lab-on-chip type applications that is an option to strictly control the position issue. If a freedom of position control is desirable, the possible solution could be an interferometric or piezo controlled positioning system.

The optoacoustic system is even more sensitive than the Raman device to accurate positioning and further experimental work is required to experimentally demonstrate the method.

7 Free-field characterization through a nanoaperture

In Paper **IV** we have applied the extraordinary transmission phenomena [26] for the characterization of free space fields. The results predict that in the device described in Fig. 7.1 the resolution of the incident beam can be maintained in transmission through the system when the incident surface has no features. Further, output side corrugations may be applied to enhance detection, particularly in low numerical aperture detection systems, due to the strong beaming effect.

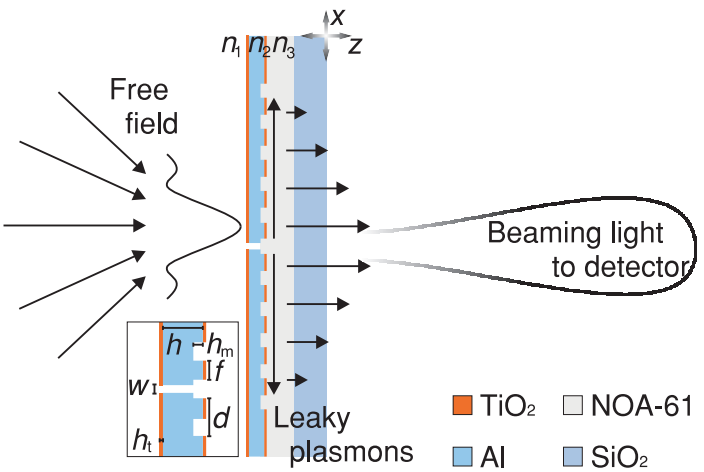

Figure 7.1: An illustration of the concept; Incident field is scanned with a system consisting of a single slit ($w = 50$ nm) on a Al film ($d = 180$ nm) and periodic modulation on the transmission side with a period $d = 380$ nm and a depth $h = 30$ nm.

Figure 7.2(a) shows the near field distribution of $|H_y|$ for the tightly focused and TM-polarized Gaussian beam, with spot size

of 400 nm, in transmission through a 50 nm wide slit in a 180 nm thick Al film. The corresponding distribution of $|H_y|$ propagating towards the far zone of the slit is shown in Fig. 7.2(b). Correspondingly, Figs. 7.2(c) and 7.2(d) show the field distribution when the out-coupling element is added on the transmission side. It is clearly seen in Fig. 7.2(c) that corrugation rapidly couples out the plasmon wave, compared to the slow attenuation of the plasmons on the smooth interface. Figure 7.2(d) shows the formation of the beaming effect behind the slit, after a few tens of wavelengths propagation distance.

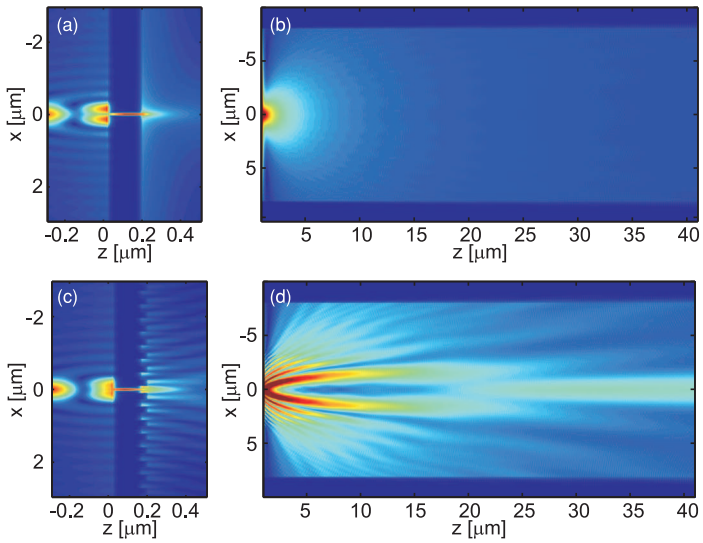

Figure 7.2: The near field distribution of $|H_y|$ field component (a) for the single slit transmission and corresponding far field (b). Respectively near (c) and far fields (d) with out-coupling corrugations.

Figure 7.3(a) shows simulated magnetic intensity profile $|H_y|^2$ for the incident field and for the probe signal under approximated experimental conditions where a tightly focused incident field is scanned perpendicularly across the slit and the transmitted intensity was recorded through a condenser lens with NA of 1.4. Here, the transmission side corrugations were shown to result in a 50% enhancement in transmission in comparison with the slit only. How-

ever, the corrugations were also designed to create the beaming effect towards zero angle allowing a greater detection sensitivity with low numerical aperture detection as shown in Fig. 7.3(b) where a 4-fold sensitivity gain for 0.16 NA system is predicted.

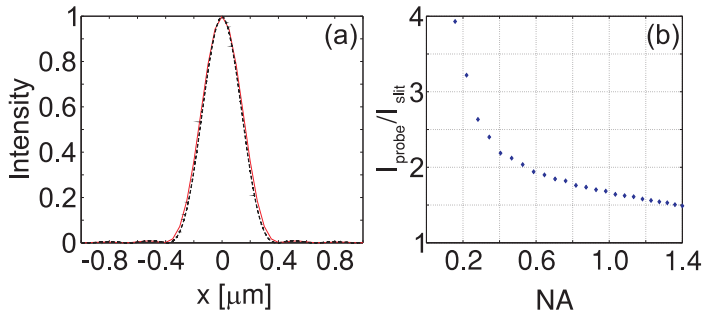

Figure 7.3: (a) Magnetic-field intensity of the incident beam (black) and the probe signal (red) in the simulated measurement conditions. (b) Dependence of the sensitivity gain factor achieved by having corrugations in the probe, plotted as a function of the collection NA.

7.1 CONFOCAL MICROSCOPY AS A PROOF OF THE CONCEPT

The device, shown in Fig. 7.1, was fabricated using the template stripping method described in section 4.5. The smooth surface was the target to minimize unwanted excitation of surface plasmons and excessive scattering from the incident surface that would result in loss of resolution. Figure 7.4(a) shows the measured signals through the slit alone and slit with corrugations, as a function of the incident beam position. The transmission was found to be about five times higher than the simulations predicted, which is most probably due to impurities on the incident surface which couple additional surface plasmon modes to enhance the signal. The same reasoning is apparent for the results shown in Figs. 7.4(b)–7.4(d) where in Fig. 7.4(b) scaling the peak signals, shown in Fig. 7.4(a), to unity predicts a decreased background noise level. Losses in the resolution in comparison with the simulated results are shown for

slit only in Fig. 7.4(c) and for the added corrugation in Fig. 7.4(d).

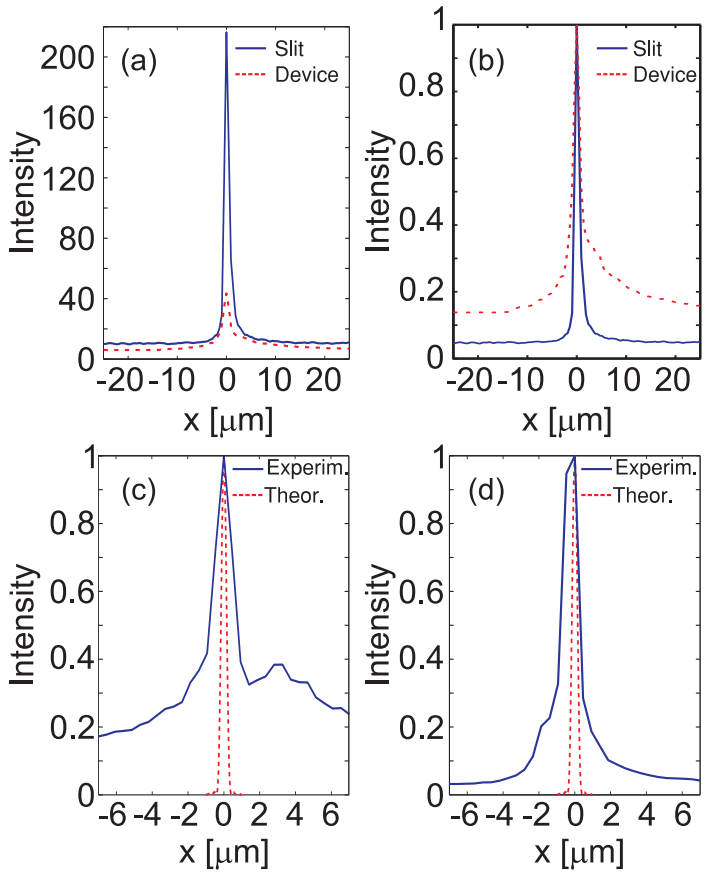

Figure 7.4: (a) Transmitted intensities as a function of the incident beam position for a single slit (dashed red) and slit with corrugation (solid blue). (b) The peak signals from (a) scaled to unity. (c) The comparison of the experimental (solid blue) and simulated (dashed red) transmitted intensity of a single slit. (d) The experimental and theoretical transmission for a slit with corrugations.

7.2 DISCUSSION

We have shown that the extraordinary transmission can be used for high resolution characterization of free fields. Even if the measured resolution and signal-to-noise ratio are not as good as we would

expect, the preliminary work gives the experimental proof of the concept.

Regardless of the fact that the fabrication of such nanoslit device is demonstrated in numerous papers with different approaches [28, 113], the most commonly applied method is based on focused ion beam fabrication, which is not a very convenient method for larger scale production. Therefore it is meaningful to further develop the electron beam lithography fabrication method. Naturally, the following step is to extend the results to a 2-dimensional nanoaperture that yields complete lateral resolution control. Further, there is no apparent limitations to apply the fabrication methods, used in this work, to fabricate other types of extraordinary optical transmission structures, for instance the ones mentioned in Refs. [28, 113].

The presented method has potential to achieve a high resolution sensor for free fields characterization. Also, with slight modifications, the device is applicable to high resolution molecular detection as described in Refs. [114, 115].

8 Conclusion

In this study, metallic and dielectric subwavelength structures alone and combined together are used to enhance the optical detection in various applications. The thesis gives a brief background for the optical phenomena, the used fabrication processes, and the design methods behind the applications.

Concerning Objective 1 in Chapter 2, the resonance waveguide grating (RWG) concept is used to produce a 530-fold enhancement in the laser induced fluorescence emission in Paper **I**. A 30-fold enhancement in the fluorescence imaging by a conventional epi-fluorescence microscope with a broadband excitation was demonstrated in Paper **II**.

In addition, the fluorescence emission scattering properties in the vicinity of the resonance waveguide grating are discussed. The results show the benefit of the RWG in the optimal emission coupling. However, this benefit is quickly lost when an emitter is drawn further away from the device, defining the optimal distance to be sub-hundred nanometers.

Further optimization of excitation field hot zone positions in the areas where molecules locate could lead even stronger enhancement in fluorescence signal. This could be relatively easily achieved by applying a free-standing RWG structure proposed in Fig. 3.4(b) in section 3.4.2. At present, in larger scale manufacturing, a fluorescence enhancing RWG platform made in polymer film by nanoimprint techniques and ALD coating would cost, say, a few tens of cents a piece.

To reach Objective 2 of Chapter 2 a new type of a slot waveguide channel method is presented in Paper **III** to enhance Raman scattering by a factor of 20 in comparison with a conventional SERS substrate in the channel configuration. This leads to a Raman enhancement factor of about 2×10^9, demonstrating that the method is highly sensitive.

Prospects for the predicted Raman enhancement device include various interesting possibilities. Current nanofabrication capabilities allow the transfer of a such device to a lab-on-chip type application with high precision channel width control. This is promising particularly in nanofluidistic devices, and also in high sensitivity environmental monitoring applications. We also expect that the concept would result in high sensitivity enhancement when applied in remote sensing with optical fibers.

A closely related approach has also been shown to be adequate to excite lateral acoustic waves with high resolution down to $\lambda/3$ and strong contrast between hot and cold spots. The method promises to fulfill Objective 3 of Chapter 2 to make the excitation of the surface acoustic waves very precise and efficient. However, experimental proof of the concept requires further work.

Finally in Paper **IV**, to meet Objective 4 of Chapter 2, an extraordinary transmission based nanoslit system was shown to be advantageous in free-field characterization. The resolution of incident beam was shown to be maintained in transmission and outcoupling corrugation can be used to enhance the collected signal and improve the signal-to-noise ratio.

Obviously, the next generation probe would have a circular aperture surrounded by circular corrugations to achieve full two-dimensional resolution. The used fabrication method is basically applicable to circular structures but alignment exposure of the slit may require some further tuning to be accurate enough. Further, the used fabrication process is useful for various other applications based on extraordinary transmission, such as plasmonic lenses.

Bibliography

[1] X. Zhang and Z. Liu, "Superlenses to overcome the diffraction limit," *Nat. Mater.* **7,** 435–441 (2008).

[2] E. Betzig, G. H. Patterson, R. Sougrat, O. W. Lindwasser, S. Olenych, J. S. Bonifacino, M. W. Davidson, J. Lippincott-Schwartz, and H. F. Hess, "Imaging Intracellular Fluorescent Proteins at Nanometer Resolution," *Science* **313,** 1642–1645 (2006).

[3] S. T. Hess, T. P. K. Girirajan, and M. D. Mason, "Ultra-High Resolution Imaging by Fluorescence Photoactivation Localization Microscopy," *Biophys. J.* **91,** 4258–4272 (2006).

[4] M. J. Rust, M. Bates, and X. Zhuang, "Sub-diffraction-limit imaging by stochastic optical reconstruction microscopy (STORM)," *Nat. Methods* **3,** 793–796 (2006).

[5] C. C. Neacsu, S. Berweger, R. L. Olmon, L. V. Saraf, C. Ropers, and M. B. Raschke, "Near-Field Localization in Plasmonic Superfocusing: A Nanoemitter on a Tip," *Nano Lett.* **10,** 592–596 (2010).

[6] J. Lindberg, "Mathematical concepts of optical superresolution," *J. Opt.* **14,** 083001 (2012).

[7] M. G. L. Gustafsson, "Surpassing the lateral resolution limit by a factor of two using structured illumination microscopy," *J. Microsc.* **198,** 82–87 (2000).

[8] L. Schermelleh, R. Heintzmann, and H. Leonhardt, "A guide to super-resolution fluorescence microscopy," *J. Cell Biol.* **190,** 165–175 (2010).

[9] M. Bertero and P. Boccacci, "Super-resolution in computational imaging," *Micron* **34,** 265–273 (2003).

[10] Z. Zalevsky, V. Mico, and J. Garcia, "Nanophotonics for optical super resolution from an information theoretical perspective: a review," *J. Nanophotonics* **3,** 032502 (2009).

[11] K. R. Catchpole and A. Polman, "Plasmonic solar cells," *Opt. Express* **16,** 21793–21800 (2008).

[12] V. E. Ferry, L. A. Sweatlock, D. Pacifici, and H. A. Atwater, "Plasmonic Nanostructure Design for Efficient Light Coupling into Solar Cells," *Nano Lett.* **8,** 4391–4397 (2008).

[13] D. A. Stuart, A. J. Haes, C. R. Yonzon, E. M. Hicks, and R. P. V. Duyne, "Biological applications of localised surface plasmonic phenomenae," *IEEE Proc. Nanobiotechnol.* **152,** 13–32 (2005).

[14] P. K. Jain, X. Huang, I. H. El-Sayed, and M. A. El-Sayed, "Review of Some Interesting Surface Plasmon Resonance-enhanced Properties of Noble Metal Nanoparticles and Their Applications to Biosystems," *Plasmonics* **2,** 107–118 (2007).

[15] R. Bardhan, W. Chen, M. Bartels, C. Perez-Torres, M. F. Botero, R. W. McAninch, A. Contreras, R. Schiff, R. G. Pautler, N. J. Halas, and A. Joshi, "Tracking of Multimodal Therapeutic Nanocomplexes Targeting Breast Cancer in Vivo," *Nano Lett.* **10,** 4920–4928 (2010).

[16] N. J. Halas, P. Nordlander, and O. Neumann, "Waste remediation," (2012), US Patent 20,120,156,102.

[17] S. Roh, T. Chung, and B. Lee, "Overview of the Characteristics of Micro- and Nano-Structured Surface Plasmon Resonance Sensors," *Sensors* **11,** 1565–1588 (2011).

[18] S. Scaranoa, M. Mascinia, A. P. F. Turner, and M. Minunn, "Surface plasmon resonance imaging for affinity-based biosensors," *Biosens. and Bioelectron.* **25,** 957–966 (2010).

[19] F. Pillet, A. Sanchez, C. Formosa, M. Séverac, E. Trévisiol, J.-Y. Bouet, and V. A. Leberre, "Dendrimer functionalization of gold surface improves the measurement of protein-DNA interactions by surface plasmon resonance imaging," *Biosens. and Bioelectron.* **43,** 148–154 (2012).

[20] S. Kawata, Y. Inouy, and P. Verma, "Plasmonics for near-field nano-imaging and superlensing," *Nat. Photonics* **3,** 388–394 (2009).

[21] K. W. Kho, S. ZeXiang, and O. Malini, "Hyper-spectral confocal nano-imaging with a 2D super-lens," *Opt. Express* **19,** 2502–2518 (2011).

[22] Z. Fang, Q. Peng, W. Song, F. Hao, J. Wang, P. Nordlander, and X. Zhu, "Plasmonic Focusing in Symmetry Broken Nanocorrals," *Nano Lett.* **11,** 893–897 (2011).

[23] S. Nie and S. R. Emory, "Probing Single Molecules and Single Nanoparticles by Surface-Enhanced Raman Scattering," *Science* **275,** 1102–1106 (1997).

[24] X. Qian, X.-H. Peng, D. O. Ansari, Q. Yin-Goen, G. Z. Chen, D. M. Shin, L. Yang, A. N. Young, M. D. Wang, and S. Nie, "In vivo tumor targeting and spectroscopic detection with surface-enhanced Raman nanoparticle tags," *Nat. Biotechnol.* **26,** 83–90 (2008).

[25] H. Im, K. C. Bantz, N. C. Lindquist, C. L. Haynes, and S.-H. Oh, "Vertically Oriented Sub-10-nm Plasmonic Nanogap Arrays," *Nano Lett.* **10,** 2231–2236 (2010).

[26] T. W. Ebbesen, H. J. Lezec, H. F. Ghaemi, T. Thio, and P. A. Wolff, "Extraordinary optical transmission through sub-wavelength hole arrays," *Nature* **391,** 667–669 (1997).

[27] C. Genet and T. W. Ebbesen, "Light in tiny holes," *Nature* **445,** 39–46 (2007).

[28] F. J. Garcia-Vidal, L. Martin-Moreno, T. W. Ebbesen, and L. Kuipers, "Light passing through subwavelength apertures," *Rev. Mod. Phys.* **82,** 729–787 (2010).

[29] R. Gordon, D. Sinton, K. L. Kavanagh, and A. G. Brolo, "A New Generation of Sensors Based on Extraordinary Optical Transmission," *Acc. Chem. Res.* **41,** 1049–1057 (2008).

[30] M. L. Juan, M. Righini, and R. Quidant, "Plasmon nano-optical tweezers," *Nat. Photonics* **5,** 349–356 (2011).

[31] M. A. Santiago-Cordoba, M. Cetinkaya, S. V. Boriskina, F. Vollmer, and M. C. Demirel, "Ultrasensitive detection of a protein by optical trapping in a photonic-plasmonic microcavity," *J. Biophoton.* **5,** 629–638 (2012).

[32] V. R. Almeida, Q. Xu, C. A. Barrios, and M. Lipson, "Guiding and confining light in void nanostructure," *Opt. Lett.* **29,** 1209–1211 (2004).

[33] C. A. Barrios, K. B. Gylfason, B. Sánchez, A. Griol, H. Sohlström, M. Holgado, and R. Casquel, "Slot-waveguide biochemical sensor," *Opt. Lett.* **32,** 3080–3082 (2007).

[34] C. A. Barrios, M. J. Bañuls, V. González-Pedro, K. B. Gylfason, B. Sánchez, A. Griol, A. Maquieira, H. Sohlström, M. Holgado, and R. Casquel, "Label-free optical biosensing with slot-waveguides," *Opt. Lett.* **33,** 708–710 (2008).

[35] Y. Fang, A. M. Ferrie, N. H. Fontaine, J. Mauro, and J. Balakrishnan, "Resonant Waveguide Grating Biosensor for Living Cell Sensing," *Biophys. J.* **91,** 1925–1940 (2006).

[36] Z. Zhang, D.-F. Lu, and Z.-M. Qi, "Application of Porous TiO_2 Thin Films as Wavelength-Interrogated Waveguide Resonance Sensors for Bio/Chemical Detection," *J. Phys. Chem. C* **116,** 3342–3348 (2012).

[37] H. N. Daghestani and B. W. Day, "Theory and Applications of Surface Plasmon Resonance, Resonant Mirror, Resonant Waveguide Grating, and Dual Polarization Interferometry Biosensors," *Sensors* **10,** 9630–9646 (2010).

[38] F. Helmchen and W. Denk, "Deep tissue two-photon microscopy," *Nat. Methods* **2,** 932–940 (2005).

[39] P. J. Caspers, G. W. Lucassen, and G. J. Puppels, "Combined In Vivo Confocal Raman Spectroscopy and Confocal Microscopy of Human Skin," *Biophys. J.* **85,** 572–580 (2003).

[40] V. Ntziachristos, "Going deeper than microscopy: the optical imaging frontier in biology," *Nat. Methods* **7,** 603–614 (2010).

[41] A. G. Podoleanu, "Optical coherence tomography," *J Microsc.* **247,** 209–219 (2012).

[42] V. Ntziachristos, J. Ripoll, L. V. Wang, and R. Weissleder, "Looking and listening to light the evolution of whole-body photonic imaging," *Nat. Biotechnol.* **23,** 313–320 (2005).

[43] H. F. Zhang, K. Maslov, G. Stoica, and L. V. Wang, "Functional photoacoustic microscopy for high-resolution and noninvasive in vivo imaging," *Nat. Biotechnol.* **24,** 848–851 (2006).

[44] K. Maslov, H. F. Zhang, S. Hu, and L. V. Wang, "Optical-resolution photoacoustic microscopy for in vivo imaging of single capillaries," *Opt. Lett.* **33,** 929–931 (2008).

[45] O. Balogun, G. D. Cole, R. Huber, D. Chinn, T. W. Murray, and J. B. Spicer, "High-spatial-resolution sub-surface imaging using a laser-based acoustic microscopy technique," *IEEE Trans. Ultrason., Ferroelectr., Freq. Control* **58,** 226–233 (2011).

[46] R. K. Leach, R. Boyd, T. Burke, H.-U. Danzebrink, K. Dirscherl, T. Dziomba, M. Gee, L. Koenders, V. Morazzani, A. Pidduck, D. Roy, W. E. S. Unger, and A. Yacoot, "The European nanometrology landscape," *Nanotechnology* **22,** 062001 (2011).

[47] URL: http://www.itrs.net/Links/2011ITRS/2011Chapters/ (valid 10th April 2013).

[48] H. Duan, H. Hu, K. Kumar, Z. Shen, and J. K. W. Yang, "Direct and reliable patterning of plasmonic nanostructures with sub-10-nm gaps," *ACS Nano* **5,** 7593–7600 (2011).

[49] D. S. Macintyre and S. Thoms, "Comparison of hydrogen silsesquioxane development methods for sub-10 nm electron beam lithography using accurate linewidth inspection," *J. Vac. Sci. Technol* **29,** 06F307 (2011).

[50] L. Mandel and E. Wolf, *Optical Coherence and Quantum Optics* (Cambridge University, 1995).

[51] M. C. Teich and B. E. Saleh, *Fundamentals of photonics* (Wiley, New York, 1991).

[52] L. D. Landau and E. M. Lifshitz, *Electrodynamics of Continuous Media* (Pergamon, Oxford, 1960).

[53] H. P. Herzig, ed., *Micro-optics: Elements, Systems and Applications* (Taylor & Francis, London, 1997).

[54] J. Turunen, Chap II in *Micro-optics: Elements, Systems and Applications.* (Taylor & Francis, London, 1997).

[55] D. M. Sullivan, *Electromagnetic Simulation Using the FDTD Method* (IEEE, New York, 2000).

[56] K. Yee, "Numerical solution of initial boundary value problems involving Maxwell's equations in isotropic media," *IEEE Trans. Antennas. Propag.* **14,** 302–307 (1966).

[57] F. Zhen, "Toward the development of a three-dimensional unconditionally stable finite-difference time-domain method," *IEEE Trans. Microw. Theory Tech.* **48,** 1550–1558 (2000).

[58] Z. Chen, *Finite Element Methods and Their Applications* (Springer, Berlin, 2005).

[59] L. Li, "Use of Fourier series in the analysis of discontinuous periodic structures," *J. Opt. Soc. Am. A* **13,** 1870–1876 (1996).

[60] L. Li, "Formulation and comparison of two recursive matrix algorithms for modeling layered diffraction gratings," *J. Opt. Soc. Am. A* **13,** 1024–1035 (1996).

[61] L. Li, "Note on the S-matrix propagation algorithm," *J. Opt. Soc. Am. A* **20,** 655–660 (2003).

[62] E. Silberstein, P. Lalanne, J.-P. Hugonin, and Q. Cao, "Use of grating theories in integrated optics," *J. Opt. Soc. Am. A* **18,** 2865–2875 (2001).

[63] J. P. Hugonin and P. Lalanne, "Perfectly matched layers as nonlinear coordinate transforms: a generalized formalization," *J. Opt. Soc. Am. A* **22,** 1844–1849 (2005).

[64] H. Kim, J. Park, and B. Lee, *Fourier Modal Method and Its Applications in Computational Nanophotonics* (Taylor & Francis, Boca Raton, FL, 2012).

[65] L. Li, "New formulation of the Fourier modal method for crossed surface-relief gratings," *J. Opt. Soc. Am. A* **14,** 2758–2767 (1997).

[66] R. W. Wood, "On a remarkable case of uneven distribution of light in a diffraction grating spectrum," *Philosophical Magazine Series 6* **4,** 396–402 (1902).

[67] A. Hessel and A. A. Oliner, "A new theory of Wood's anomalies on optical gratings," *Appl. Opt.* **10,** 1275–1297 (1965).

[68] E. Popov, L. Mashev, and D. Maystre, "Theoretical study of the anomalies of coated dielectric gratings," *J. Mod. Opt.* **33,** 607–619 (1986).

[69] S. S. Wang, R. Magnusson, J. S. Bagby, and M. G. Moharam, "Guided-mode resonances in planar dielectric-layer diffraction gratings," *J. Opt. Soc. Am. A* **7,** 1470–1474 (1990).

[70] R. Magnusson and S. S. Wang, "New principle for optical filters," *Appl. Phys. Lett.* **61,** 1022–1024 (1992).

[71] D. Rosenblatt, A. Sharon, and A. A. Friesem, "Resonant Grating Waveguide Structures," *IEEE J. Quantum Elect.* **33,** 2038–2059 (1997).

[72] Y. Ding and R. Magnusson, "Resonant leaky-mode spectral-band engineering and device applications," *Opt. Express* **12,** 5661–5674 (2004).

[73] T. Saastamoinen, T. Alasaarela, A. Lehmuskero, I. Vartiainen, N. Heikkilä, and M. Kuittinen, "Resonance waveguide reflectors with semi-wide bandwidth at the visible wavelengths," *Opt. Express* **19,** 2126–2132 (2011).

[74] N. Zaytseva, W. Miller, V. Goral, J. Hepburn, and Y. Fang, "Microfluidic resonant waveguide grating biosensor system for whole cell sensing," *Appl. Phys. Lett.* **98,** 163703 (2011).

[75] N. Ganesh, I. D. Block, P. C. Mathias, W. Zhang, E. Chow, V. Malyarchuk, and B. T. Cunningham, "Leaky-mode assisted fluorescence extraction: application to fluorescence enhancement biosensors," *Opt. Express* **16,** 21626–21640 (2008).

[76] A. Saari, G. Genty, M. Siltanen, P. Karvinen, P. Vahimaa, M. Kuittinen, and M. Kauranen, "Giant enhancement of second-harmonic generation in multiple diffraction orders from sub-wavelength resonant waveguide grating," *Opt. Express* **18,** 12298–12303 (2010).

[77] T. Ning, H. Pietarinen, O. Hyvärinen, R. Kumar, T. Kaplas, M. Kauranen, and G. Genty, "Efficient second-harmonic generation in silicon nitride resonant waveguide gratings," *Opt. Express* **37,** 4269–4271 (2012).

[78] A. Otto, "Excitation of nonradiative surface plasma waves in silver by the method of frustrated total reflection," *Z. Phys.* **216,** 398–410 (1968).

[79] Q. Cao and P. Lalanne, "Negative Role of Surface Plasmons in the Transmission of Metallic Gratings with Very Narrow Slits," *Phys. Rev. Lett.* **88,** 057403 (2002).

[80] M. Fleischmann, P. J. Hendra, and A. J. McQuillan, "Raman spectra of pyridine adsorbed at a silver electrode," *Chem. Phys. Lett.* **26,** 163–166 (1974).

[81] C. R. Yonzon, D. A. Stuart, X. Zhang, A. D. McFarland, C. L. Haynes, and R. P. Van Duyne, "Towards advanced chemical and biological nanosensors – An overview," *Talanta* **67,** 438–448 (2005).

[82] F. Yan, M. B. Wabuyele, G. D. Griffin, A. A. Vass, and T. Vo-Dinh, "Surface-Enhanced Raman scattering detection of chemical and biological agent simulants," *IEEE Sensors* **5,** 665–670 (2005).

[83] B. Sharma, R. R. Frontiera, A.-I. Henry, E. Ringe, and R. P. V. Duyne, "SERS: Materials, applications, and the future," *Mater. Today* **15,** 16–25 (2012).

[84] M. Moskovits, "Surface-enhanced spectroscopy," *Rev. Mod. Phys* **57,** 783–826 (1985).

[85] P. L. Stiles, J. A. Dieringer, N. C. Shah, and R. P. V. Duyne, "Surface-Enhanced Raman Spectroscopy," *Annu. Rev. Anal. Chem.* **1,** 601–626 (2008).

[86] A. Otto, "The chemical (electronic) contribution to surface-enhanced Raman scattering," *J. Raman Spec.* **36,** 497–509 (2005).

[87] B. N. J. Persson, K. Zhao, and Z. Zhang, "Chemical Contribution to Surface-Enhanced Raman Scattering," *Phys. Rev. Lett.* **96,** 207401 (2006).

[88] J. A. Rogers, A. A. Maznev, M. J. Banet, and K. A. Nelson, "Optical generation and characterization of acoustic waves in

thin films: fundamentals and applications," *Annu. Rev. Mater. Sci.* **30,** 117–157 (2000).

[89] S. Ramanathana and D. G. Cahilla, "High-resolution picosecond acoustic microscopy for non-invasive characterization of buried interfaces," *J. Mater. Res.* **21,** 1204–1208 (2006).

[90] T. J. Grimsley, J. Ma, Q. Miao, A. V. Nurmikko, and H. J. Maris, "Picosecond Ultrasonic and Heat Flow Measurements with Enhanced Sensitivity," *Chin. J. Phys.* **49,** 176–183 (2011).

[91] H. J. Maris and A. V. Nurmikko, "Opto-acoustic methods and apparatus for performing high resolution acoustic imaging and other sample probing and modification operations," (2009), US Patent 7,624,640.

[92] J. Laukkanen, *Fabrication of Metallic Micro- and Nanostructures for Optical Solutions*, PhD thesis (The University of Eastern Finland, Joensuu, 2010).

[93] W. Hu, K. Sarveswaran, M. Lieberman, and G. H. Bernstein, "Sub-10 nm electron beam lithography using cold development of poly(methylmethacrylate)," *J. Vac. Sci. Technol. B* **22,** 1711–1716 (2004).

[94] J. Reinspach, M. Lindblom, O. von Hofsten, M. Bertilson, H. M. Hertz, and A. Holmberg, "Cold-developed electron-beam-patterned ZEP 7000 for fabrication of 13 nm nickel zone plates," *J. Vac. Sci. Technol. B* **27,** 2593–2596 (2009).

[95] A. Lehmuskero, M. Kuittinen, and P. Vahimaa, "Refractive index and extinction coefficient dependence of thin Al and Ir films on deposition technique and thickness," *Opt. Express* **15,** 10744–10752 (2007).

[96] H. W. Lehmann and K. Frick, "Optimizing deposition parameters of electron beam evaporated TiO2 films," *Appl. Opt.* **27,** 4920–4924 (1988).

[97] T. Alasaarela, *Atomic Layer Deposited Titanium Dioxide in Optical Waveguiding Applications*, PhD thesis (Aalto University, Espoo, 2011).

[98] M. Ritala, K. Kukli, A. Rahtu, P. I. Räisänen, M. Leskelä, T. Sajavaara, and J. Keinonen, "Atomic Layer Deposition of Oxide Thin Films with Metal Alkoxides as Oxygen Sources," *Science* **288,** 319–321 (2000).

[99] S. Y. Chou, P. R. Krauss, and P. J. Renstrom, "Nanoimprint lithography," *J. Vac. Sci. Technol. B* **14,** 4129–4133 (1996).

[100] S. Y. Chou, P. R. Krauss, W. Zhang, L. Guo, and L. Zhuang, "Sub-10 nm imprint lithography and applications," *J. Vac. Sci. Technol. B* **15,** 2897–2904 (1997).

[101] L. J. Heyderman, H. Schift, C. David, B. Ketterer, M. A. der Maur, and J. Gobrecht, "Nanofabrication using hot embossing lithography and electroforming," *Microelectron. Eng.* **57–58,** 375–380 (2001).

[102] S. H. Ahn and L. J. Guo, "High-Speed Roll-to-Roll Nanoimprint Lithography on Flexible Plastic Substrates," *Adv. Mater.* **20,** 2044–2049 (2008).

[103] M. Hegner, P. Wagner, and G. Semenza, "Ultralarge atomically flat template-stripped Au surfaces for scanning probe microscopy," *Surf. Sci.* **291,** 39–46 (1993).

[104] P. Nagpal, N. C. Lindquist, S.-H. Oh, and D. J. Norris, "Ultrasmooth patterned metals for plasmonics and metamaterials," *Science* **31,** 594–597 (2009).

[105] J. Pietarinen, V. Kalima, T. T. Pakkanen, and M. Kuittinen, "Improvement of UV-moulding accuracy by heat and solvent assisted process," *Microelectron. Eng.* **85,** 263–270 (2008).

[106] J.-J. Greffet, R. Carminati, K. Joulain, J.-P. Mulet, S. Mainguy, and Y. Chen, "Coherent emission of light by thermal sources," *Nature* **416,** 61–64 (2001).

[107] B. J. Lee, C. J. Fu, and Z. M. Zhang, "Coherent thermal emission from one-dimensional photonic crystals," *Appl. Phys. Lett.* **87,** 071904 (2005).

[108] D. J. Stephens and V. J. Allan, "Light Microscopy Techniques for Live Cell Imaging," *Science* **300,** 82–86 (2003).

[109] J. A. Steyer and W. Almers, "A real-time view of life within 100 nm of the plasma membrane," *Nature Rev. Mol. Cell Biol.* **2,** 268–275 (2001).

[110] J. D. Jackson, Chap 9 in *Classical Electrodynamics* (John Wiley & Sons, 1999).

[111] E. C. Le Ru, E. Blackie, M. Meyer, and P. G. Etchegoin, "Surface Enhanced Raman Scattering Enhancement Factors: A Comprehensive Study," *J. Phys. Chem. C* **111,** 13794–13803 (2007).

[112] J. Zhou, S. Xu, W. Xu, B. Zhao, and Y. Ozaki, "In situ nucleation and growth of silver nanoparticles inmembranematerials: a controllable roughened SERS substrate with high reproducibility," *J. Raman Spectrosc.* **40,** 31–37 (2009).

[113] C. Zheng, X. Cui, and C. Yang, "Surface-wave-enabled darkfield aperture for background suppression during weak signal detection," *PNAS* **107,** 9042–9048 (2010).

[114] C. Chen, F. Clemente, R. Kox, L. Lagae, G. Maes, G. Borghs, and P. Van Dorpe, "Raman scattered photon transmission through a single nanoslit," *Appl. Phys. Lett.* **96,** 061108 (2010).

[115] K.-L. Lee, S.-H. Wu, C.-W. Lee, and P.-K. Wei, "Sensitive biosensors using Fano resonance in single gold nanoslit with periodic grooves," *Opt. Express* **19,** 24530–24539 (2011).

Jussi Rahomäki

Subwavelength photonics for enhanced optical imaging

This thesis is dedicated to subwavelength photonics methods to enhance optical imaging for various schemes. Experimental and theoretical approaches, along fabrication methods, are concidered to push sensitivity and resolution of the examined sensing applications. The proposed methods have potential on the fields of fluorescence and Raman detection, optoacoustic metrology, and characterization of focal-region optical fields.

UNIVERSITY OF
EASTERN FINLAND

Publications of the University of Eastern Finland
Dissertations in Forestry and Natural Sciences

ISBN: 978-952-61-1192-6 (printed)
ISSNL: 1798-5668
ISSN: 1798-5668
ISBN: 978-952-61-1193-3 (pdf)
ISSNL: 1798-5668
ISSN: 1798-5676